Smart Agricultural Technology 9 (2024) 100619

Contents lists available at ScienceDirect

Smart Agricultural Technology

journal homepage: www.journals.elsevier.com/smart-agricultural-technology

Innovative multi-temporal evapotranspiration forecasting using empirical fourier decomposition and bidirectional long short-term memory

Masoud Karbasi [a,b], Mumtaz Ali [c], Gurjit S. Randhawa [d,*], Mehdi Jamei [a,e,f], Anurag Malik [g], Syed Hamid Hussain Shah [a,h], Melanie Bos [i], Qamar Zaman [j], Aitazaz Ahsan Farooque [a,k,*]

[a] Canadian Centre for Climate Change and Adaptation, University of Prince Edward Island, St Peters Bay, PE, Canada
[b] Water Engineering Department, Faculty of Agriculture, University of Zanjan, Zanjan, Iran
[c] UniSQ College, University of Southern Queensland 4305 QLD, Australia
[d] School of Computer Science, University of Guelph, Guelph, ON, Canada
[e] Faculty of Civil Engineering and Architecture, Shahid Chamran University of Ahvaz, Ahvaz, Iran
[f] New Era and Development in Civil Engineering Research Group, Scientific Research Center, Al-Ayen University, Thi-Qar, Nasiriyah 64001, Iraq
[g] Punjab Agricultural University, Regional Research Station, Bathinda, 151001, Punjab, India
[h] College of Engineering, University of Saskatchewan, Saskatoon, SK, Canada
[i] Nature Conservancy of Canada, Fredericton NB, Canada
[j] Faculty of Agriculture, Dalhousie University, Truro, NS, Canada
[k] Faculty of Sustainable Design Engineering, University of Prince Edward Island, Charlottetown, PE, Canada

ARTICLE INFO

Keywords:
Evapotranspiration
Empirical fourier decomposition
Machine learning
Deep learning
Climate adaptation
Feature selection

ABSTRACT

Reference evapotranspiration (ET_o) is an essential environmental variable that is intimately significant to agriculture. Managing water and crop planning relies heavily on precise forecasting of ET_o. This research used a novel time series decomposition technique, Empirical Fourier Decomposition (EFD), to forecast ET_o accurately. Four machine learning techniques were used to forecast ET_o using decomposed lagged ET_o values. The input data source was from Prince Edward Island (PEI) weather stations (Harrington and St Peters Stations). First, autocorrelation analysis was performed to determine effective lags. Then, ET_o data were decomposed using EFD, and lagged data was created based on EFD results. The Kbest feature selection algorithm was used to choose effective inputs, reducing the training time. The accuracy of models was evaluated using different statistical metrics such as correlation coefficient (R) and root mean square error (RMSE). The results showed that using EFD decomposition can significantly improve forecast accuracy. The comparison between different machine learning models showed that the deep learning-based model (Bidirectional LSTM (Long Short Term Memory)) (R = 0.956, RMSE= 0.451 mm/day for Harrington station and R = 0.956, RMSE= 0.451 mm/day for St Peters station) performed better than the Generalized Regression Neural Network (GRNN), K-nearest neighbor (KNN), and Random Forest (RF) models. Finally, the best model (EFD-Bidirectional LSTM) was used to forecast multi-temporal ET_o at both stations. Results showed that the developed model can forecast ET_o for up to 28 days with reasonable accuracy. However, the accuracy of multi-step ahead forecasting decreases when evapotranspiration values are high, as the models tend to underestimate these values. The findings of this study can assist in accurately calculating crop water requirements and help farmers optimize their irrigation schedules.

1. Introduction

The significance of reference evapotranspiration (ET_o) lies in its ability to facilitate the movement of water from soil, water, and vegetation surfaces to the atmosphere. Evapotranspiration represents the summation of plant transpiration and soil, plant, and open surface evaporation. Evapotranspiration is a complicated phenomenon influenced by various environmental factors, with meteorological parameters as its primary driver. Although numerous analytical methods have been suggested to estimate ET_o, the Penman-Monteith model developed by the Food and Agricultural Organisation of the United Nations (FAO) has gained widespread acceptance as the standard for calculating ET_o [1,

* Corresponding authors.
E-mail addresses: randhawg@uoguelph.ca (G.S. Randhawa), afarooque@upei.ca (A.A. Farooque).

https://doi.org/10.1016/j.atech.2024.100619
Received 3 September 2024; Received in revised form 22 October 2024; Accepted 23 October 2024
Available online 28 October 2024

2]. This equation makes use of climatic data obtained from weather stations, encompassing parameters such as minimum and maximum temperatures, humidity, wind speed, sunlight hours, and radiation. The non-stationarity nature of the ET_o time series leads to difficulties in forecasting future values [3].

The ET_o is the main driver of soil moisture, relative humidity, transpiration, plant water stress, and terrestrial fluxes of latent heat. The actual evapotranspiration (ET_{act}) is calculated by multiplying the crop coefficient with the ET_o [1,4]. The crop coefficient is a strong function of leaf area index (LAI), water stress, and salinity stress factors.

In various regions and seasons, early warning systems can become unreliable, making it challenging to accurately estimate soil moisture and runoff. This difficulty arises from the potential underestimation or overestimation of Evapotranspiration (ET_o). Terrestrial evapotranspiration rates have increased due to global warming and atmospheric demands. The implications to agricultural production systems and the economy without efficient prediction of ET_o during early crop stages are obvious. The development of an efficient evapotranspiration prediction model has become imperative and compulsory to adaptively manage water resources and sustainably produce foods. If information related to the evapotranspiration coupling of land and atmosphere is missing, forecasting drought magnitude, intensity, and patterns cannot be performed.

Currently, the state-of-the-art Penman-Monteith equation uses climatic variables as an input, including wind speed, relative humidity, air temperature, and solar radiation data [5]. At a point, the magnitude of ET_o can be calculated using other known parameters, but the knowledge of future ET_o cannot be captured with physical models. Consequently, powerful machine learning and artificial intelligence models may be employed to generate precise predictions and offer an additional understanding of this critical land-atmosphere coupling variable [6–10].

Hydrological parameters (ET_o is one of the important parameters) have been predicted and modeled using time series analysis techniques such as seasonal auto-regressive integrated moving average (SARIMA) [11–13]. In light of these challenges, various researchers adopted effective modeling techniques that leverage data-driven machine learning. These modeling approaches consider supervised and unsupervised learning algorithms, which are sub-classified as relevance vector machines (RVM), multiple regression methods (MRM), artificial neural networks (ANN), and support vector machines (SVM). For example, the weekly ET_o has shown good performance using ANN, as reported by [11]. In another study, the results of using state-of-the-art empirical models Penmann, Turc, and Hargreaves were compared with ANN-based daily estimated ET_o [14]. The presence of non-stationary data makes predictions challenging; however, the Artificial Neural Network (ANN) model can be used effectively in this context [15,16]. Hydrological parameters modeling and prediction have been performed frequently by many researchers using RVM. Due to a single output, these models are considered as further steps after forecasting. In that case, predictions at distributed time steps are considered to get the multiple outputs using a multivariance relevance vector machine (MVRVM). In recent years, the application of different deep learning models in time series forecasting has become very popular[17, 18]. The deep-bidirectional LSTMs are a variant of the LSTM (Long Short Term Memory) models that have been previously described, in which two LSTMs are fitted to the input data [19]. The input sequence is subjected to an LSTM in the initial round (forward layer). In the second round, the LSTM model (i.e., backward layer) is supplied with the reverse form of the input sequence. The LSTM's accuracy will be enhanced due to the improved understanding of long-term dependencies resulting from its application twice.

Over the past decade, wavelet transformation has been widely regarded as a valuable technique for analyzing temporal variations, trends, and periodicities. The structure of the physical process that needs to be modeled can be diagnosed to extract the signal local representation with time and frequency using the wavelet transforms. The application of wavelet analysis for a wide range of fields, including water resources, has received considerable attention [20]. The fluctuations in global hydrological signals as well as time-varying relationships among variables, have been improved due to the application of wavelets, as reported in different studies.

Researchers have developed hybrid models using the coupling technique of wavelet transforms with artificial intelligence and time series models. Firstly, the wavelet transform approach decomposes the time series into various temporal scales. After that, regression models are applied. This hybrid technique shows better results than the traditional time series prediction and analysis approach [21]. This hybrid approach of wavelet decomposition and neural networks has improved ET_o modeling and prediction, as reported by [15]. Similarly, a wavelet-neural network was developed by [22] using the combination of neural network and wavelet transformation approach, and this model has the capability to forecast ET_o 1 day ahead. Based on the non-stationarity and non-linearity nature of the evapotranspiration signal, the hybrid wavelet model is a good alternative solution for estimating and forecasting the evapotranspiration problem.

The Empirical Fourier Decomposition (EFD) stands out as a method for decomposition that outperforms techniques like the Empirical Wavelet Transform (EWT) and the Fourier Decomposition Method (FDM). EFD excels in providing consistent decomposition results for signals with non-stationary modes and closely spaced frequencies. Unlike EWT and FDM, EFD maintains its accuracy in challenging scenarios by addressing the mode mixing issue related to EWT through an enhanced frequency spectrum segmentation approach. Furthermore, EFD resolves the inconsistency problem of FDM by merging segmentation with a filter bank, ensuring a precise decomposition process. With its ability to effectively capture both time and frequency information, EFD is a tool for analyzing stationary signals while offering computational efficiency compared to alternative methods. In essence, by combining the strengths of Fourier theory with techniques, EFD emerges as an asset for signal analysis purposes [23]. Recently, the EFD algorithm and its combination with machine learning techniques were used to forecast time series data [24,25]. Kumar and Yadav (2024) used a hybrid model (EFD-LSTM-GWO) to forecast wind speed. Their results showed that the application of EFD instead of EWT and VMD could improve the performance of machine learning methods in terms of wind speed forecasting. Jamei et al. (2024) applied EFD for drought forecasting in Iran. According to their results, the EFD signal decomposition technique can significantly improve the accuracy compared with single machine learning techniques.

Agricultural planning is significantly influenced by the precise forecasting of ETo. Although previous research has employed a variety of hybrid modeling and machine learning techniques, the potential to overcome non-stationarities in ETo time series data is demonstrated by the utilization of more sophisticated signal decomposition techniques prior to modeling. Nevertheless, wavelet transformations or other decomposition methods are the primary approaches employed by current hybrid methods. Empirical Fourier Decomposition (EFD) is a relatively new algorithm that has demonstrated superiority over conventional techniques in the analysis of non-stationary signals with closely spaced frequencies. It has the potential to provide advantages over alternatives by effectively capturing time-frequency information through an enhanced segmentation approach. Nevertheless, EFD has not yet been thoroughly investigated in the context of hydrologic time series forecasting and compared to hybrid modeling approaches. The main contribution of the current study is the application of Empirical Fourier Decomposition (EFD), BiLSTM networks and K-best feature selection for ET_o forecasting in a single framework while previous studies mainly utilized wavelet or other conventional decomposition methods in conjunction with simple machine learning algorithms. The objectives of this investigation are as follows:

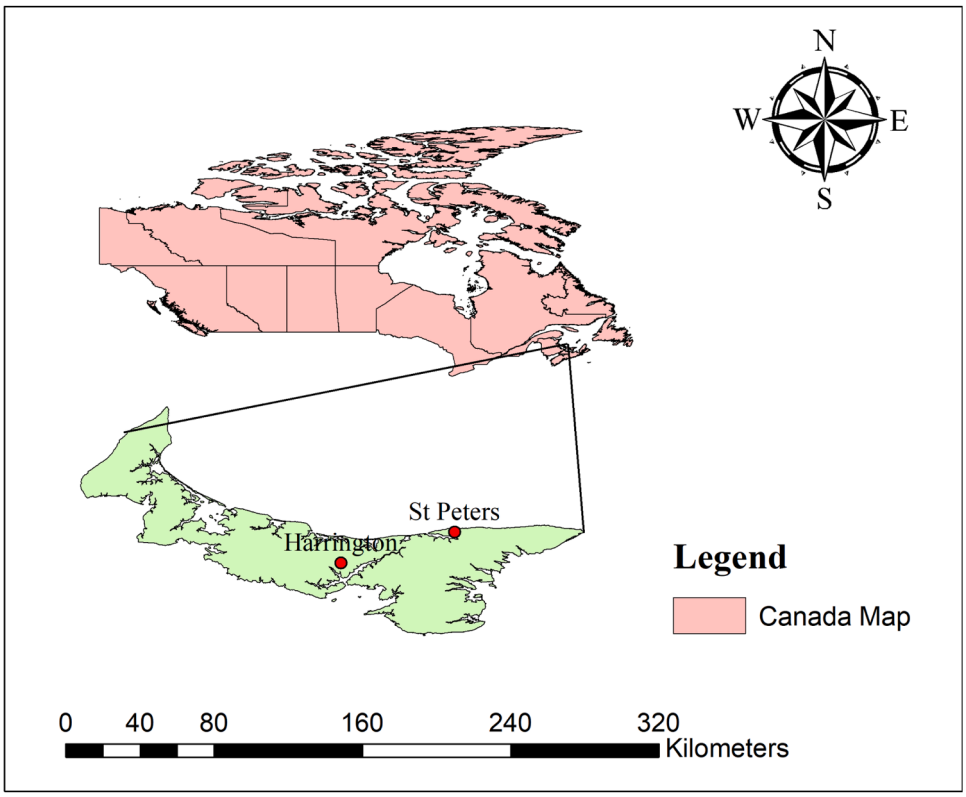

Fig. 1. Weather station locations on Prince Edward Island (PEI) used for climatic data.

1. Develop a hybrid forecasting framework that combines Empirical Fourier Decomposition (EFD) with Bidirectional Long Short-Term Memory (BiLSTM) networks for multi-temporal ET_o forecasting.
2. Implement K-best feature selection to optimize the input feature space for the BiLSTM model and improve forecast accuracy.
3. Decompose historical ET_o time series data into intrinsic mode functions using EFD and train the BiLSTM model on the decomposed signals.
4. To validate its effectiveness, compare the proposed EFD-BiLSTM-Kbest framework against other machine learning techniques (Random Forest, K-Nearest Neighbors, general regression neural network).
5. Provide insights into how the proposed framework helps address non-stationarities in ET_o time series for more accurate short-term forecasts.

The overall goal is to advance multi-temporal ET_o forecasting through a novel signal decomposition-driven hybrid modeling framework leveraging EFD, BiLSTM networks, and optimized feature selection.

2. Methodology

2.1. Study area

Two stations on Prince Edward Island (PEI) were selected to test and evaluate the developed models (Fig. 1). PEI is a province in eastern Canada that has a marine climate that is thought to be mild and is heavily impacted by the nearby waters. PEI receives an average of 890 mm of rain and 290 cm of snow annually. In January, the average low temperature is −7 °C, while in July, the average high temperature is 19 °C [26]. Agriculture is an important industry in PEI, and it leads nationally in potato (*Solanum tuberosum*) production, providing 23 % of the national volume and contributing over 44 % to total farm cash receipts in the province [27].

Table 1
Descriptive statistics of climate condition and ET_o values in 2011 −2017.

Station	Metric	RH (%)	Wind Speed (m s^{-1})	T_{max} (°C)	T_{min} (°C)	ET_o (mm/day)
Harrington	Mean	78.1	15.1	10.5	2.2	1.9
	Standard deviation	10.4	6.1	10.6	9.9	1.5
	Coefficient of variation	0.1	0.4	1.0	4.5	0.8
	Minimum	37.6	0.0	−17.7	−26.0	0.1
	Maximum	99.4	43.6	32.5	21.3	8.2
	Q1	71.0	10.6	1.5	−4.8	0.7
	Median	78.7	14.4	10.6	2.5	1.5
	Q3	86.1	18.6	19.7	11.0	2.8
	Skewness	−0.4	0.7	−0.2	−0.3	0.9
	Kurtosis	−0.1	0.7	−1.0	−0.7	0.1
St Peters	Mean	79.1	15.8	10.5	2.3	1.9
	Standard deviation	10.0	6.3	10.4	9.6	1.5
	Coefficient of variation	0.1	0.4	1.0	4.1	0.8
	Minimum	38.7	1.0	−17.0	−23.8	0.1
	Maximum	98.0	45.0	32.0	21.6	9.3
	Q1	72.5	11.0	1.8	−4.5	0.7
	Median	80.0	15.0	10.6	2.6	1.5
	Q3	86.9	19.4	19.6	10.5	2.9
	Skewness	−0.5	0.8	−0.1	−0.3	0.9
	Kurtosis	−0.1	0.7	−1.0	−0.7	0.4

2.2. Data description

Data was collected from automatic weather stations over the period of 2011–2017. Table 1 illustrates the data's descriptive statistics (mean, standard deviation, quartiles (Q1, median, and Q3), skewness, and

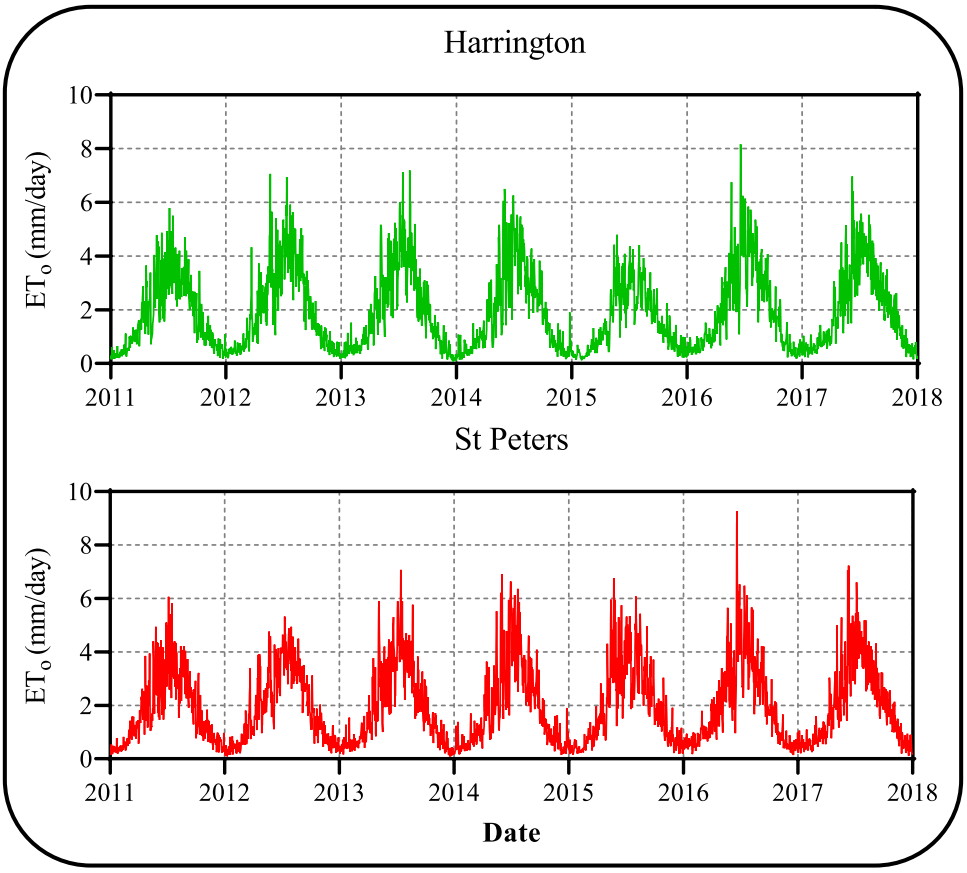

Fig. 2. Time series of reference evapotranspiration in Harrington and St peters stations.

kurtosis). Data for relative humidity (RH), wind speed, minimum temperature (T_{min}), and maximum temperature (T_{max}) were collected from the two weather stations. ET_o values were calculated using the famous Penman-Monteith FAO56 (PMF-56) equation [2]. According to Table 1, the mean values of ET_o are 1.89 and 1.92 mm/day for Harrington and St Peters stations, respectively. Due to the fact that skewness and kurtosis are between −1 and 1, the data distribution is near normal. Fig. 2 shows the fluctuations of ET_o time series data for Harrington and St Peters stations.

2.3. Empirical fourier decomposition (EFD)

Throughout the years, numerous methods for signal decomposition, such as empirical wavelet transform, Fourier decomposition method, and variational mode decomposition, have been introduced as solutions to address the issues of mode mixing and inconsistency. However, these approaches are not sufficient to resolve the problems mentioned earlier. The EFD method addresses these concerns through the implementation of an enhanced Fourier spectrum segmentation technique and a zero-phase filter bank (Zhou et al., 2022). Furthermore, by using the concept of the lower minima technique, the improved segmentation approach is projected, which divides the frequency range, $[0, \pi]$ into N contiguous frequency segments. Matching frequencies in the primary N largest values in the sorted series are represented as $\Omega_1,\ \Omega_2, \ldots \Omega_N$. Likewise, $\Omega_0 = 0$ and $\Omega_{N+1} = \pi$ are defined. The boundaries of each segment are computed as [23]:

$$\omega_n = \begin{cases} \arg\min \breve{X}_n(\omega) & \text{if } 0 \le n \le N \text{ and } \Omega_n \ne \Omega_{n+1} \\ \Omega_n & \text{if } 0 \le n \le N \text{ and } \Omega_n = \Omega_{n+1} \end{cases} \tag{1}$$

In which, $\breve{X}_n(\omega)$ represents the Fourier spectrum magnitudes amid Ω_n and Ω_{n+1}, which achieves the improved segmentation technique. Afterward, a zero-phase filter bank is created by using frequency segments received from the improved segmentation technique. From now on, all the major Fourier spectrum components in the segment are retained by the zero-phase filter and neglect the other Fourier spectrum components outside the segment [23]. Fourier transform of a signal to be decomposed $f(t)$ is defined as:

$$\widehat{f}(\omega) = \int_{-\infty}^{\infty} f(t) e^{-j\omega t}\, dt \tag{2}$$

a zero-phase filter bank can be built by $\widehat{\mu}_n(\omega)$:

$$\widehat{\mu}_n(\omega) = \begin{cases} 1 & \text{if } \omega_{n-1} \le |\omega| \le \omega_n \\ 0 & \text{otherwise} \end{cases} \tag{3}$$

where $1 \le n \le N$ and values of ω_n are calculated by Eq. (1). Filtered signals that are associated to $\widehat{\mu}_n(\omega)$ are estimated as:

$$\widehat{f}_n(\omega) = \widehat{\mu}_n(\omega)\widehat{f}(\omega) = \begin{cases} \widehat{f}(\omega) & \text{if } \omega_{n-1} \le |\omega| \le \omega_n \\ 0 & \text{otherwise} \end{cases} \tag{4}$$

The components that have decomposed in the time domain can be acquired by employing the inverse Fourier transform:

$$\begin{aligned} f_n(t) = F^{-1}[\widehat{f}_n(\omega)] &= \int_{-\infty}^{\infty} \widehat{f}_n(\omega) e^{j\omega t}\, d\omega \\ &= \int_{-\omega_n}^{-\omega_{n-1}} \widehat{f}(\omega) e^{j\omega t}\, d\omega + \int_{\omega_{n-1}}^{\omega_n} \widehat{f}(\omega) e^{j\omega t}\, d\omega \end{aligned} \tag{5}$$

Finally, the reunited signal is intended as a summation of all decomposed components:

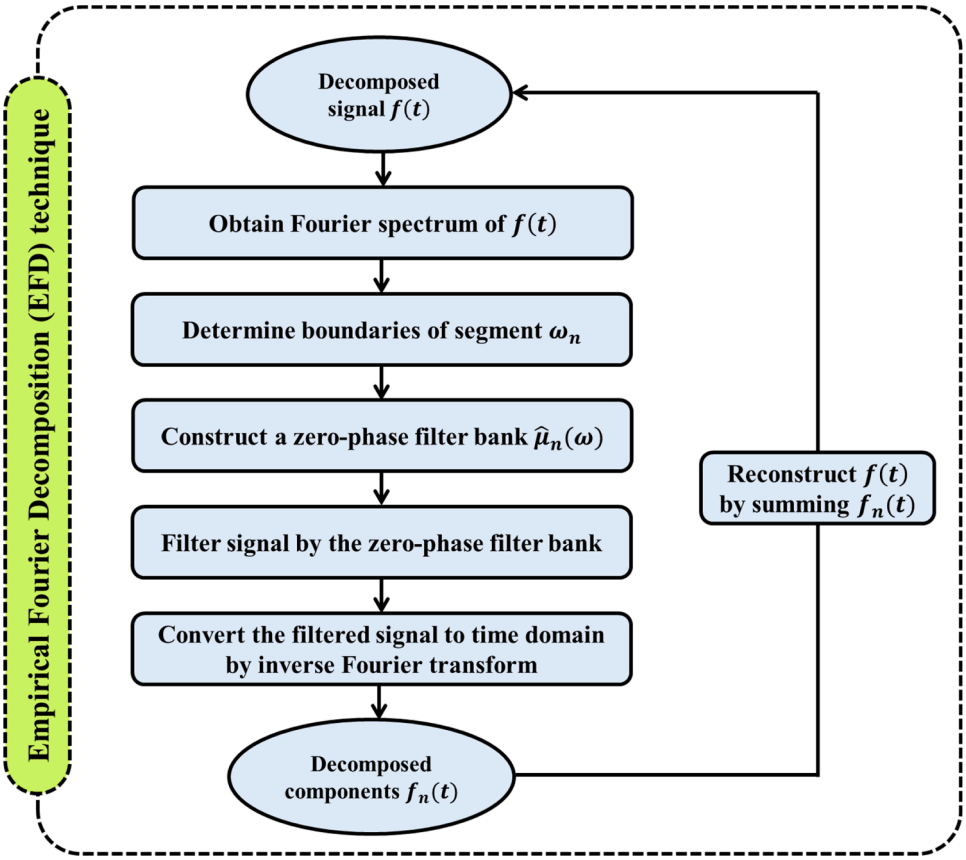

Fig. 3. Workflow chart of the EFD.

$$\widetilde{f}(t) = \sum_{n=1}^{N} f_n(t) \tag{6}$$

This study exploited the EFD technique for decomposing the ET_o data series at Harrington and St Peters stations. Fig. 3 shows the systematic flowchart of the EFD.

2.4. Kbest feature selection

Univariate statistical tests were employed in our feature selection procedure to reduce the number of characteristics. To be more precise, the univariate statistical test parameter was established as the Chi-Square test via the function SelectKBest provided by the Scikit-Learn module [28]. The Chi-Square statistic is calculated across each feature of the training sample using the results of this test.

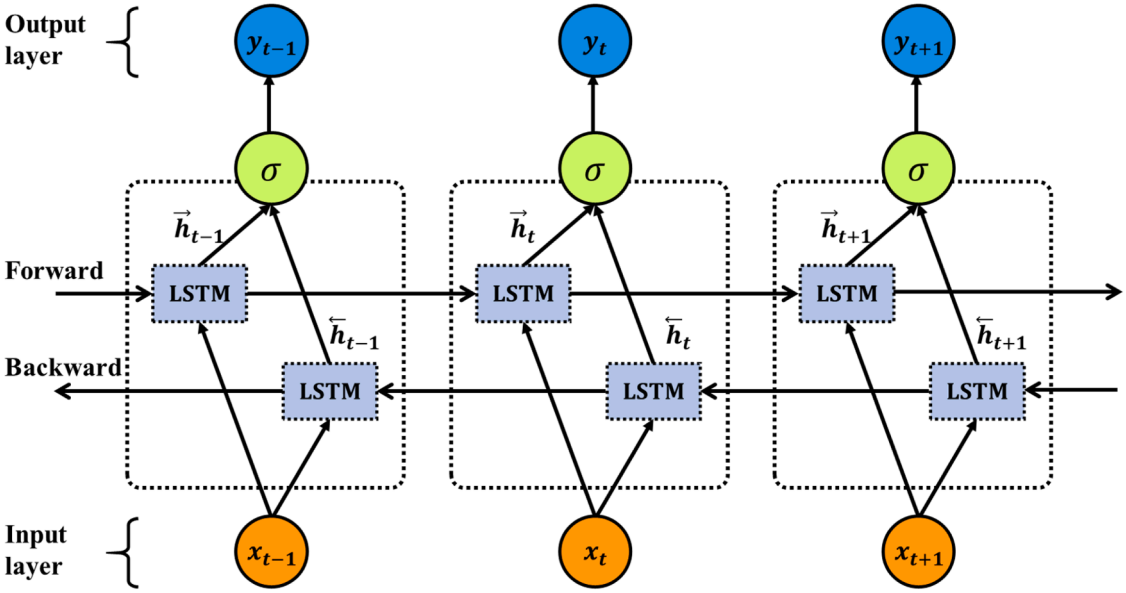

Fig. 4. The Bi-LSTM model's input and output layers' structure.

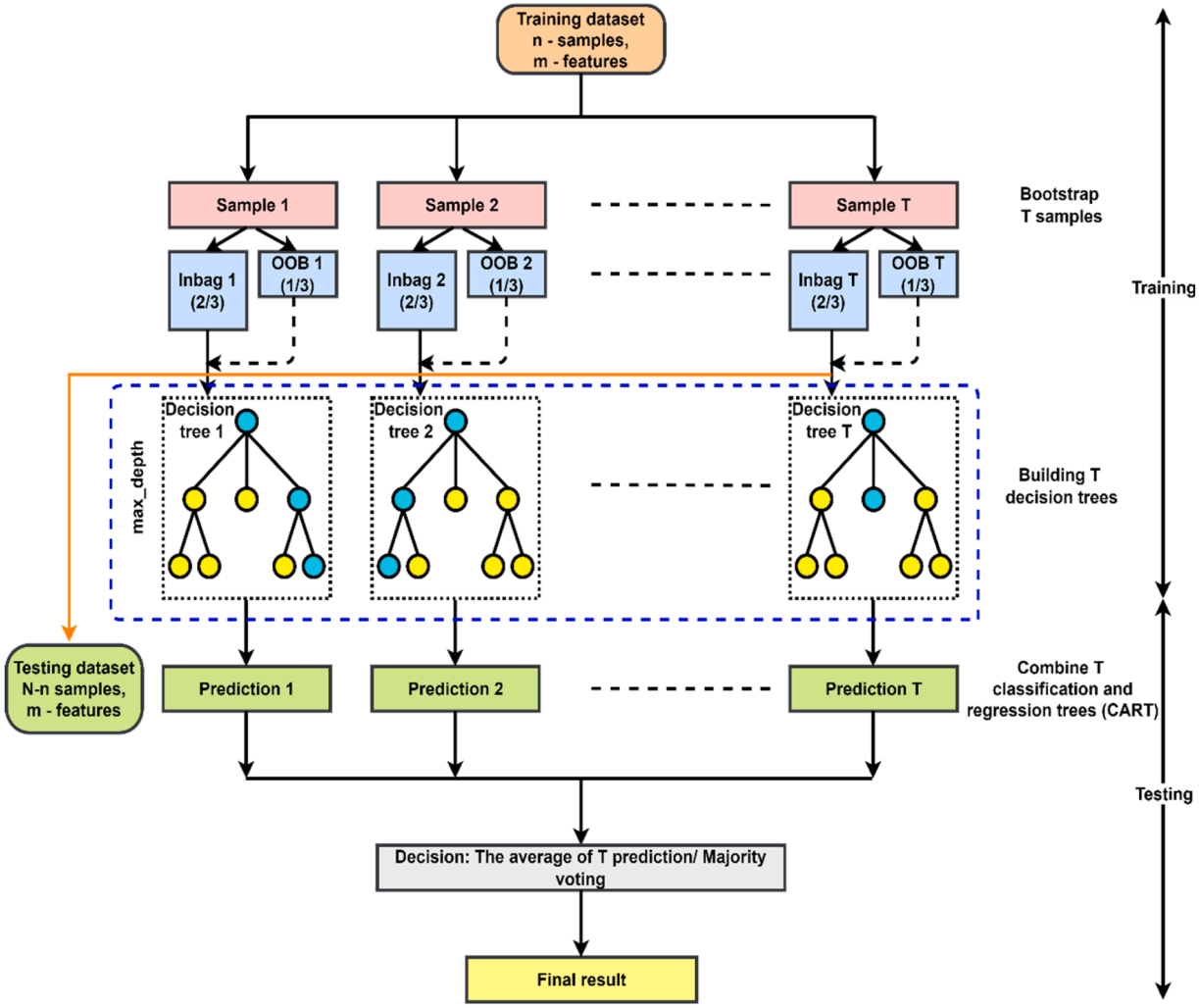

Fig. 5. Architecture of the RF model.

A low Chi-Square number indicates that the characteristic is unrelated to the classes. On the other hand, a high score indicates that the characteristic is closely connected to the classes and can offer crucial data for identifying the instances. SelectKBest will choose the first K features from the training dataset that have the highest scores, as the function's name implies [29].

Through the use of the following equation, the $\chi 2$ value for n sets of expected and actual frequencies may be calculated [30]:

$$\chi^2 = \sum_{i=1}^{n} \frac{(OF_i - EF_i)^2}{EF_i} \tag{7}$$

The OF_i stands for the observed frequency for the feature F's i th value, whereas the EF_i stands for the predicted frequency for the same feature F's i th value.

2.5. Machine learning methods

2.5.1. BiDirectional LSTM

The Bi-LSTM model is an extended version of the traditional LSTM model, which handles both forward and backward dependencies and extracts the information of multiple meanings [19,31]. Globally, this model received massive applications in different fields of science and engineering. The Bi-LSTM model is very advantageous for learning the temporal-spatial related data pictures comprehensively, finding the association of time predictions with past-present-future time series and future-present-past time series, and appropriate for the sequence-to-point prediction [32]. Fig. 4 demonstrates the typical network of the Bi-LSTM model. The forward state $\left(\overrightarrow{h_t}\right)$, backward state $\left(\overleftarrow{h_t}\right)$, and output (y_t) of the Bi-LSTM are defined as [33]:

$$\overrightarrow{h_t} = \sigma\left(U_{\overrightarrow{h}} x_t + W_{\overrightarrow{h}} \overrightarrow{h}_{t-1} + b_{\overrightarrow{h}}\right) \tag{8}$$

$$\overleftarrow{h_t} = \sigma\left(U_{\overleftarrow{h}} x_t + W_{\overleftarrow{h}} \overrightarrow{h}_{t-1} + b_{\overleftarrow{h}}\right) \tag{9}$$

$$y_t = \sigma\left(V_{\overrightarrow{h}} \overrightarrow{h_t} + V_{\overleftarrow{h}} \overleftarrow{h_t} + b_y\right) \tag{10}$$

Here, U and W are the weight matrices, σ is the sigmoid function, and b is the bias vector. This study exploited the Bi-LSTM model for ET_o prediction at Harrington and St Peters stations.

2.5.2. General regression neural network (GRNN)

The general regression neural network (GRNN) was proposed by Specht (1991) as a type of supervised network. The GRNN model is capable of producing outputs that possess continuous values. The GRNN is composed of an input layer, a hidden layer, a summation layer, and an output layer. In the hidden layer, each training pattern is associated with one hidden neuron. The GRNN is a network with memory that gives values of continuous variables and converges to the underlying

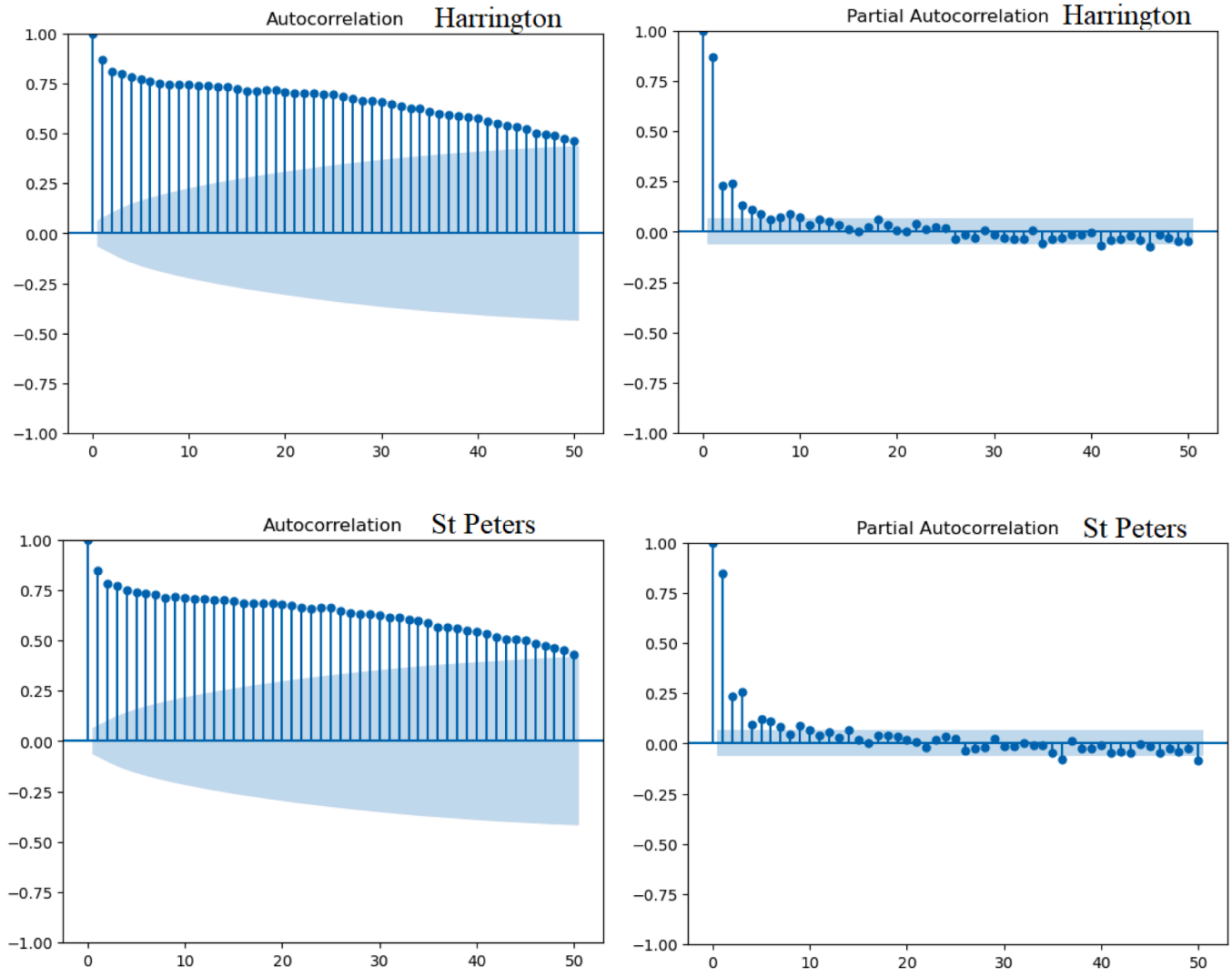

Fig. 6. Autocorrelation and partial autocorrelation of ET_o time series at Harrington and St Peters stations.

regression surface [34].

The input layer is responsible for gathering and transmitting information to the pattern layer. The pattern layer is employed during the training procedure to carry out clustering. Normally, the number of neurons in the pattern layer is equal to the number of data sets in the training pairs. Subsequently, it traverses the layer of summation. This particular layer comprises solely of two designated neurons, namely S-Summation neurons and D-Summation neurons. The following equation is derived from the two summation layer neurons (Ghritlahre and Prasad, 2018).

$$S = \sum_{i=1}^{n} W_i exp[-F(x, x_i)] \text{ and } D = \sum_{i=1}^{n} exp[-F(x, x_i)] \quad (11)$$

By splitting the results of the summation layer, the output layer (the fourth layer) is able to provide a predicted value y for the input vector x, as shown below.

$$Y(X) = \frac{S}{D} = \frac{\sum_{i=1}^{n} W_i exp[-F(x, x_i)]}{\sum_{i=1}^{n} exp[-F(x, x_i)]} \quad (12)$$

The variable n represents the total number of training patterns, while Wi denotes the weight that connects the ith neuron in the pattern layer to the summation layer. The Gaussian F function mentioned in Equations is defined as follows:

$$F(x, x_i) = \sum_{j=1}^{p} \left(\frac{x_j - x_{ij}}{\sigma_j}\right)^2 \quad (13)$$

The variable "p" denotes the dimension of the input vector. The symbols x_j and x_{ij} denote the jth element of the variable x and the ith element of the variable x_i, respectively. The spread factor is commonly denoted as σ_j.

2.5.3. *Random forest (RF)*

Random forest (RF) is a tree-based ensemble machine-learning algorithm proposed by Breiman (2001) to develop forecasting models for classification and regression problems [35,36]. The RF model utilized the bagging (bootstrap aggregating) idea to ensemble a group of decision trees with precise alteration [37]. In RF, random binary trees are generated with a subset of the observations through the bootstrapping method. The dataset included in the bag is referred to as "*inbag*" where each tree is grown from about 2/3rd of each bootstrap sample, and the dataset not in the bag is stated as "out-of-bag" (OOB) from the bootstrap sample and utilized to appraise the general problems [37]. The final predictions are obtained by averaging (majority voting) all the decision trees, which results in the RF model. Fig. 5 illustrates the conceptual diagram of the RF model. Additionally, the proper tuning of the hyperparameters (i.e., *ntree*: number of trees, *mtry*: number of randomly nominated variables at each node; and *nodesize*: minimum number of

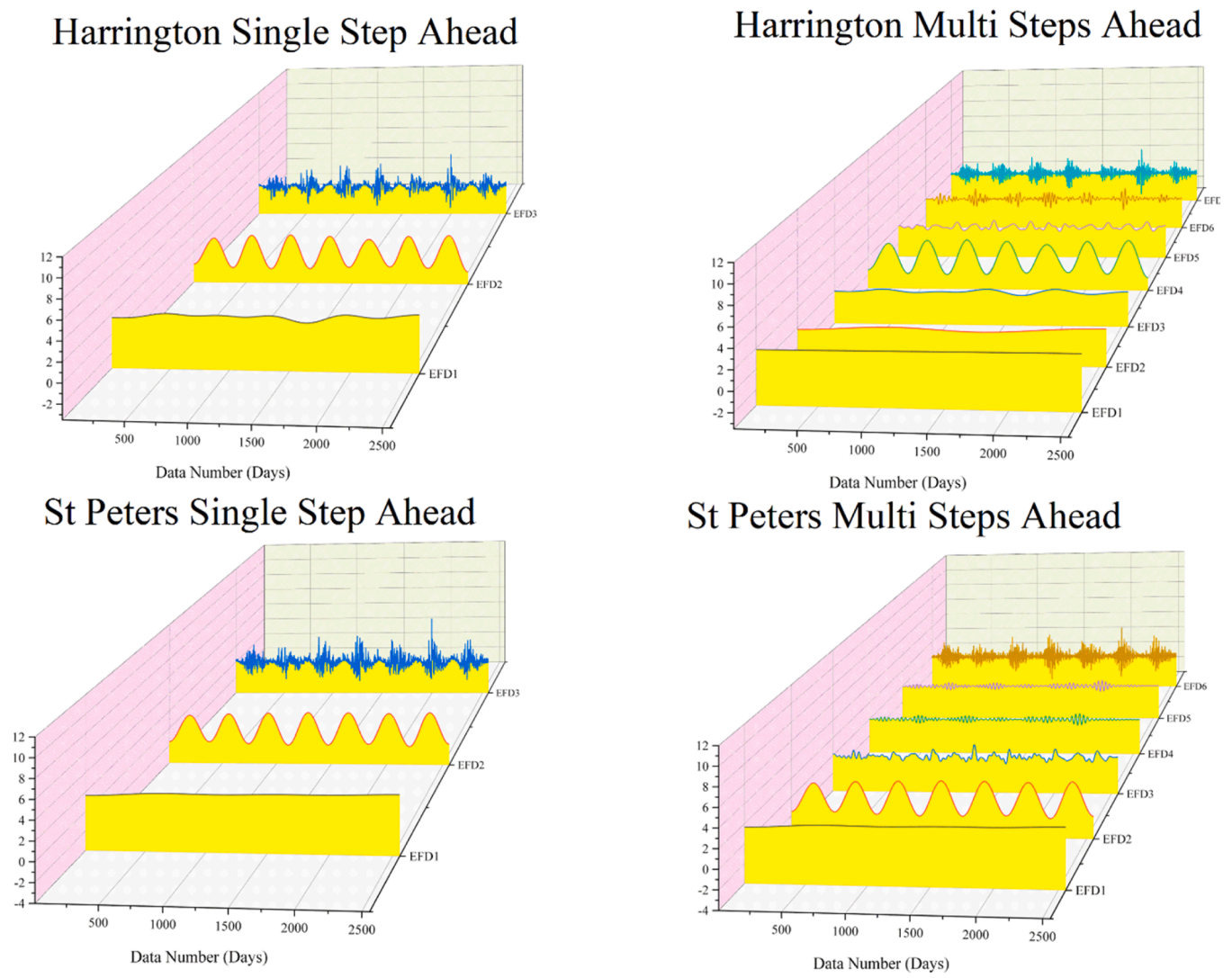

Fig. 7. Plots of decomposed ET_o time series using empirical Fourier decomposition technique for single and multi-step (days) forecasting.

observations at the terminal nodes of the trees) enhances the performance of the RF model [38]. Breiman (2001) and Tyralis et al. (2019) can offer more information about the RF model.

2.5.4. K-Nearest neighbors (KNN)

The kNN algorithm [39] is a supervised machine-learning technique that can be used for classification and regression. This algorithm tries to classify new samples alongside those that are similar. This method assigns newly generated data from a previously generated sample set to the cluster with the closest (k) distance. For regression issues, the KNN model takes the average distance between the subject and its nearest neighbors as the regression value. The Euclidean distance is the most frequently utilized distance metric. It is computed according to the formula presented in the following equation:

$$d(x_i, x_j) = \sqrt{\sum_{k=1}^{N} (x_{ik} - x_{jk})^2} \quad (14)$$

Where N represents the number of input features, x_{ik} and x_{jk} denote the n^{th} feature values for the i^{th} and j^{th} observations. After calculating the distances, the KNN algorithm chooses the K neighbors with the shortest distances. The expected value of the new observation is then computed as the mean (or median) of the values of the target variable in the K nearest neighbors [40].

2.6. Model development

Here, the model development stages are comprehensively expressed to provide a multi-process intelligent system for multi-temporal daily ET_o forecasting based on a self-feature strategy for the two stations on PEI. The datasets used to construct the forecasting models using daily data of ET_o from 2011 to 2017 (2011–2015 for training and 2016–2017 for test models). In this regard, the provided hybrid framework combines the Kbest feature selection, empirical Fourier decomposition (EDF), and the Bidirectional LSTM deep learning technique, which uses the filtered decomposed antecedent information of the ET_o as the input feature. The present study involves the development of four complementary algorithms, namely EFD-Bi-LSTM, EFD-KNN, EFD-RF, and EFD-GRNN, and four standalone counterpart models (e.i., Bi-LSTM, KNN, RF, and GRNN). The models have been constructed using MATLAB 2023a and Python 3.10 programming environments. The EFD decomposition technique, GRNN, and RF models are executed using the MATLAB programming language, while the Kbest feature selection technique, Bi-LSTM, and KNN are conducted using the Python programming language. The computational simulations are executed on a computer system equipped with a Laptop core i7 Processor operating at a frequency of 2.6 GHz and a memory capacity of 32 GB. Notably, the BI-LSTM model was provided by the TensorFlow open-source library. In contrast, the Kbest feature selection and KNN model were executed using the Scikit-learn

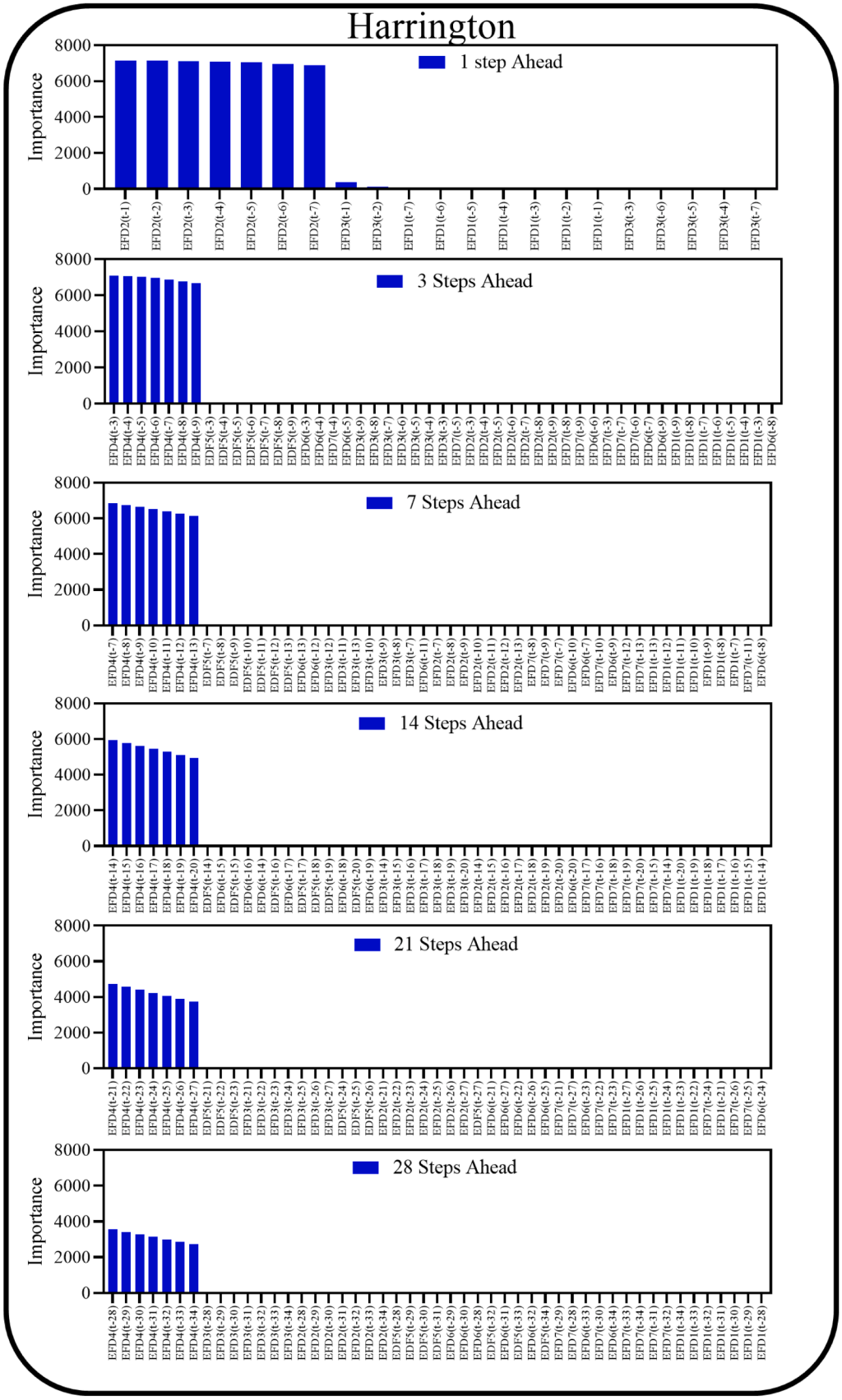

Fig. 8. Results of feature selection using the Kbest Method for Harrington (upper) and St Peters (lower) stations (EFDs are Intrinsic Mode functions (IMFs) derived from Empirical Fourier Decomposition. Numbers in parenthesis stand for time lag).

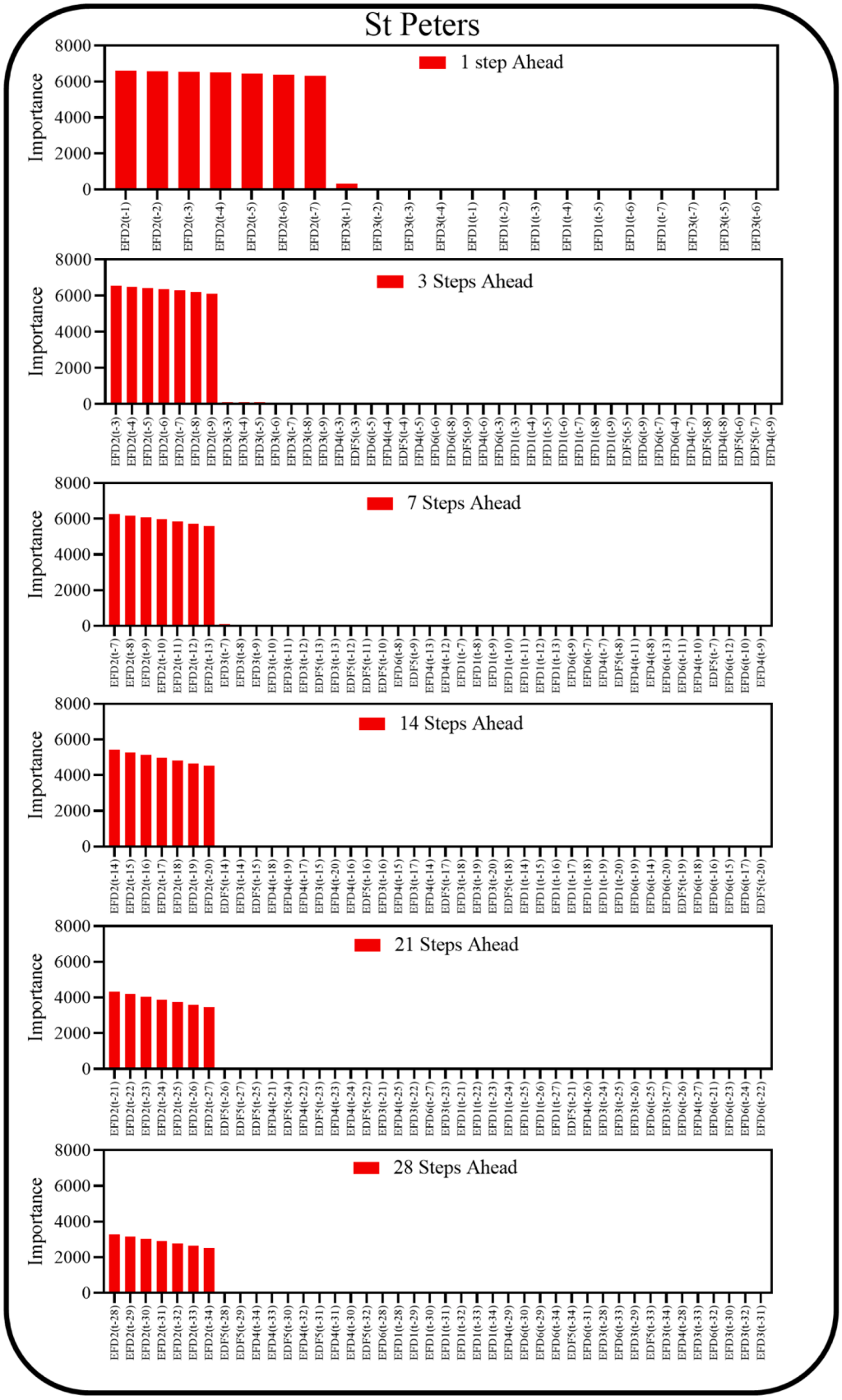

Fig. 8. (*continued*).

Table 2
Effective input parameters selected by Kbest for different time steps.

	Time Steps	Selected effective inputs by Kbest feature selection
Harrington	1	*EFD2(t-1), EFD2(t-2), EFD2(t-3), EFD2(t-4), EFD2(t-5), EFD2(t-6), EFD2(t-7)
	3	EFD4(t-3), EFD4(t-4), EFD4(t-5), EFD4(t-6), EFD4(t-7), EFD4(t-8), EFD4(t-9)
	7	EFD4(t-7), EFD4(t-8), EFD4(t-9), EFD4(t-10), EFD4(t-11), EFD4(t-12), EFD4(t-13)
	14	EFD4(t-14), EFD4(t-15), EFD4(t-16), EFD4(t-17), EFD4(t-18), EFD4(t-19), EFD4(t-20)
	21	EFD4(t-21), EFD4(t-22), EFD4(t-23), EFD4(t-24), EFD4(t-25), EFD4(t-26), EFD4(t-27)
	28	EFD4(t-28), EFD4(t-29), EFD4(t-30), EFD4(t-31), EFD4(t-32), EFD4(t-33), EFD4(t-34)
St Peters	1	EFD2(t-1), EFD2(t-2), EFD2(t-3), EFD2(t-4), EFD2(t-5), EFD2(t-6), EFD2(t-7)
	3	EFD2(t-3), EFD2(t-4), EFD2(t-5), EFD2(t-6), EFD2(t-7), EFD2(t-8), EFD2(t-9)
	7	EFD2(t-7), EFD2(t-8), EFD2(t-9), EFD2(t-10), EFD2(t-11), EFD2(t-12), EFD2(t-13)
	14	EFD2(t-14), EFD2(t-15), EFD2(t-16), EFD2(t-17), EFD2(t-18), EFD2(t-19), EFD2(t-20)
	21	EFD2(t-21), EFD2(t-22), EFD2(t-23), EFD2(t-24), EFD2(t-25), EFD2(t-26), EFD2(t-27)
	28	EFD2(t-28), EFD2(t-29), EFD2(t-30), EFD2(t-31), EFD2(t-32), EFD2(t-33), EFD2(t-34)

* EFDs are Intrinsic Mode functions (IMFs) derived from Empirical Fourier Decomposition. Numbers in parenthesis stand for time lag.

[28] open-source library of the Python platform. The model configuration stages are described as follows:

1. Since, in the current research, just the ET_o signal is available as the input feature, it is required that the most influential lags of ET_o be characterized in the first preprocessing step. Autocorrelation (ACF) and spatial auto-correlation (PACF), the most popular time series analysis statistical techniques, were employed to specify the significant time-lagged components in St Peters and Harrington stations. Partial correlation is a statistical measure that assesses the connection between two variables while accounting for the influence of one or more additional variables. It is beneficial to eliminate the influence of other variables that may confuse the relationship in order to isolate the clear connection between the two variables of interest. Fig. 6 illustrates the ACF and PACF between prospective antecedent information sub-sequences and ET_o. The blue shaded area denotes the significance threshold with 95 % confidence. The analysis statistically shows that the first seven lags of the ET_o (ET_o(t-1), ET_o(t-2), …, ET_o(t-7)) have more correlation with the original signal of ET_o.
2. According to the high non-stationary ET_o signal, a powerful decomposition technique aiming to enhance the accuracy is required. The EFD technique is one of the most novel decomposition schemes based on the Fourier series, which can capture the complexity and noise of ET_o. One of the remarkable properties of the EFD decomposition technique, along with the signal non-stationary reduction, is the simplicity of tuning the setting parameters [23]. The most important setting parameter in the EFD is the mode decomposition number (MDN), which can be optimized for the RMSE criterion. Fig. 7 demonstrates the decomposed antecedent information sub-sequences related to the single and multi-step (days) ahead forecasting of the ET_o, considering (MDN=3 and 7) in Harrington and (MDN=3 and 6) in St Peters stations, respectively. Application of different MDNs showed that in single-time step forecasting, there is no difference using MDN=3 and MDN =6,7, so due to an increase in computational cost, MDN=3 is considered for single-time step forecasting. At the end of this preprocessing step, the selected lags for each station and horizon are applied to the decomposed ET_o sub-signals. These lagged data are used to forecast future time steps. In the next stage, the lagged data will be analyzed, and important lags will be selected by the Kbest feature selection technique.
3. Feature selection is a crucial step in ML techniques and data analysis. The feature selection process holds significant importance in constructing ML models, as it decreases complexity, enhances accuracy, and improves interpretability. One of the efficient feature selection approaches is the Kbest feature selection algorithm. The Kbest feature selection mechanism filtering is based on the Chi-squared-based importance factors. In this research, as the third signal preprocessing, various antecedent sub-components in each scenario (multi-temporal horizons) are examined to select relevant variables and lags for forecast using the Kbest. Fig. 8 depicts the important factors of all the EFD-decomposed sub-sequences for the 1, 3, 7, 14, 21, and 24 days ahead of ET_o extraction by the Kbest scheme. In Fig. 8, EFD_1, EFD_2, …, and EFD_7 mean the main ET_o time series decomposition level from 1 to 7. Table 2 represents the best inputs for each time step which is obtained from the Kbest feature selection algorithm. Eventually, these selected features are then applied to feed the ML model to obtain results for the hybrid model.
4. An essential aspect of the preparation process for AI-based prediction systems is the adjustment of tuning parameters linked to the models, with the aim of attaining the highest levels of accuracy and efficiency [41]. The outputs of Bi-LSTM-based techniques, due to the complexity of architecture, are greatly influenced by the learning rate, activation function, number of hidden layers, and number of hidden nodes. The grid search technique was addressed to find the optimal hyperparameters of Bi-LSTM, KNN, and RF models. Table 3 reports the most favorable architectures for the understudy ML models in hybrid and standalone frameworks.

Table 3
Results of fine-tuning for the forecasting of ET_o.

Study site	Models	Tuning parameter models
Harrington	EFD-BiLSTM	LSTM Layers: 1 Number of Neurons: 40, Epochs: 53, Learning Rate: 0.003, Batch Size: 32
	EFD-RF	N_Estimators: 110, Max-Depth:10
	EFD-GRNN	Spread:0.05
	EFD-KNN	Number of Neighbours: 15
	BiLSTM	LSTM Layers: 1 Number of Neurons: 20, Epochs: 46, Learning Rate: 0.001, Batch Size: 32
	RF	N_Estimators: 70, Max-Depth:3
	GRNN	Spread: 0.125
	KNN	Number of Neighbours: 25
St Peters	EFD-BiLSTM	LSTM Layers: 1 Number of Neurons: 40, Epochs: 49, Learning Rate: 0.001, Batch Size: 32
	EFD-RF	N_Estimators: 200, Max-Depth:30
	EFD-GRNN	Spread:0.05
	EFD-KNN	Number of Neighbours: 10
	BiLSTM	LSTM Layers: 1 Number of Neurons: 30, Epochs: 30, Learning Rate: 0.001, Batch Size: 32
	RF	N_Estimators: 70, Max-Depth:5
	GRNN	Spread: 0.125
	KNN	Number of Neighbours: 15

Fig. 9 provides a schematic flowchart to reveal the forecasting stages

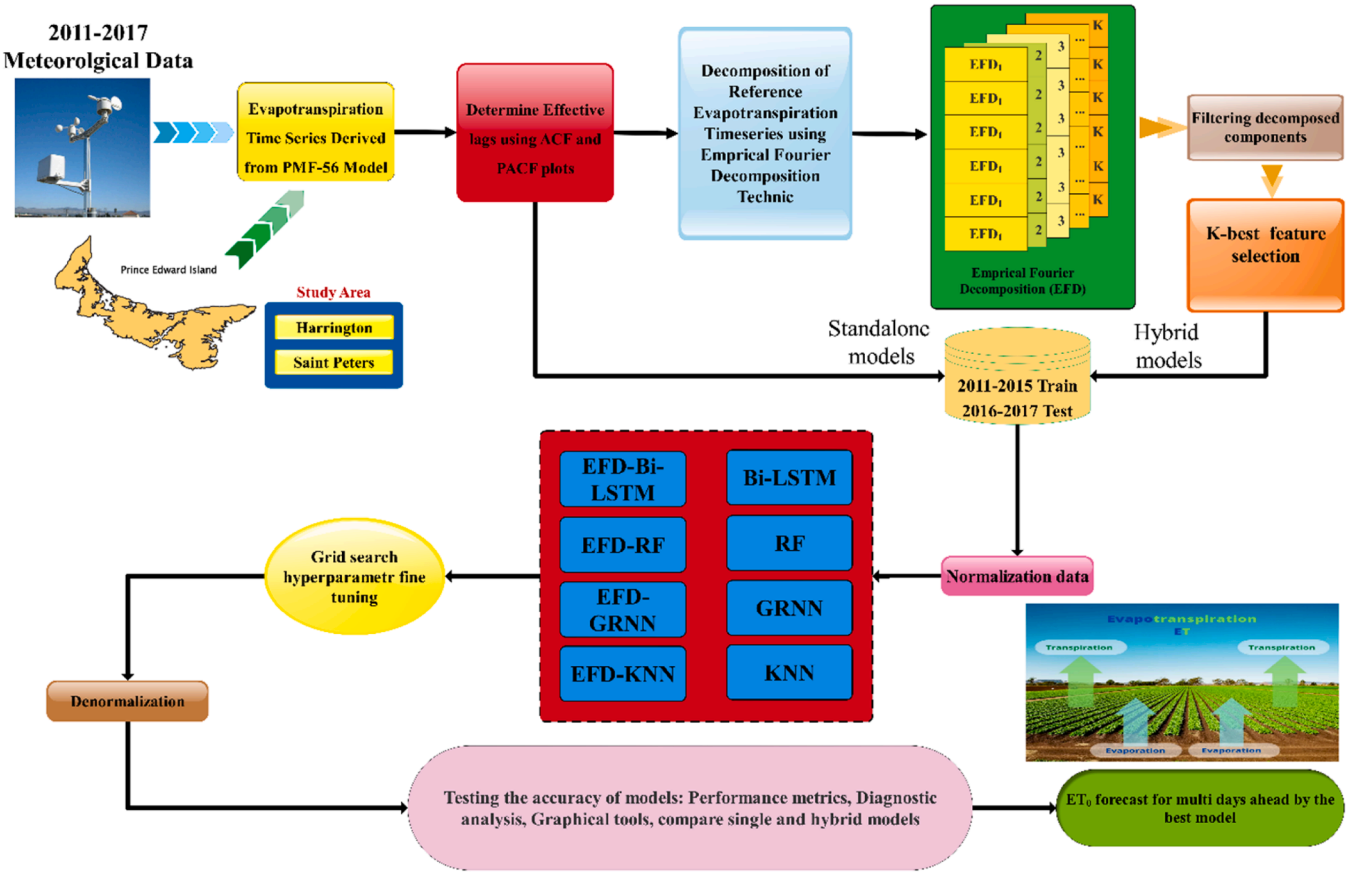

Fig. 9. Workflow of reference evapotranspiration forecasting using empirical fourier transform (EFD).

for the ET_o.

2.7. Evaluation metrics

One of the key elements in the application of machine learning models is the evaluation process, which involves the use of statistical criteria. The research employed a set of seven distinct criteria (Correlation Coefficient (R), Root Mean Square Error (RMSE), Mean Absolute Percentage Error (MAPE), Theil's inequality coefficients (U_1, U_2) [42], Kling Gupta Efficiency (KGE) [43] and uncertainty with 95% confidence level (U_{95} %)) to evaluate and compare the accuracy of the models. The following is the mathematical description of the used metrics [44]:

$$R = \frac{\sum_{i=1}^{N}\left(ET_{o,i} - \overline{ET_o}\right)\left(ET_{p,i} - \overline{ET_p}\right)}{\sqrt{\sum_{i=1}^{N}\left(ET_{o,i} - \overline{ET_o}\right)^2 \sum_{i=1}^{N}\left(ET_{p,i} - \overline{ET_p}\right)^2}} \quad (15)$$

$$RMSE = \sqrt{\frac{1}{N}\sum_{i=1}^{N}\left(ET_{o,i} - ET_{p,i}\right)^2} \quad (16)$$

Table 4
Evaluation metrics for one step ahead ET_o forecasting in Harrington station.

Model	Data	*R	RMSE (mm/day)	MAPE%	KGE	U_1	U_2	U_{95} %
GRNN	Train	0.918	0.572	34.631	0.843	0.126	0.244	1.117
	Test	0.884	0.723	30.303	0.801	0.148	0.284	1.011
RF	Train	0.978	0.326	17.007	0.878	0.072	0.140	0.904
	Test	0.885	0.715	30.346	0.811	0.145	0.281	1.981
KNN	Train	0.950	0.462	21.935	0.851	0.102	0.198	1.280
	Test	0.887	0.713	28.855	0.801	0.146	0.281	1.974
BiLSTM	Train	0.977	0.314	14.849	0.912	0.068	0.135	0.871
	Test	0.897	0.676	28.137	0.855	0.135	0.266	1.873
EFD-GRNN	Train	0.975	0.319	18.839	0.947	0.069	0.137	0.626
	Test	0.914	0.626	25.771	0.878	0.126	0.246	0.757
EFD-RF	Train	0.927	0.535	23.511	0.915	0.116	0.230	1.484
	Test	0.944	0.513	21.319	0.893	0.104	0.202	1.412
EFD-KNN	Train	0.948	0.455	22.294	0.902	0.100	0.195	1.262
	Test	0.941	0.537	21.922	0.870	0.110	0.211	1.466
EFD-BiLSTM	Train	0.946	0.466	23.830	0.930	0.100	0.200	1.288
	Test	**0.956**	**0.451**	**18.921**	**0.935**	**0.090**	**0.178**	**1.251**

* R: Correlation Coefficient, RMSE: Root Mean Square Error, MAPE: Mean Absolute Percentage Error, U_1 and U_2: Theil's inequality coefficients, KGE: Kling Gupta Efficiency, U_{95} % uncertainty with 95% confidence.

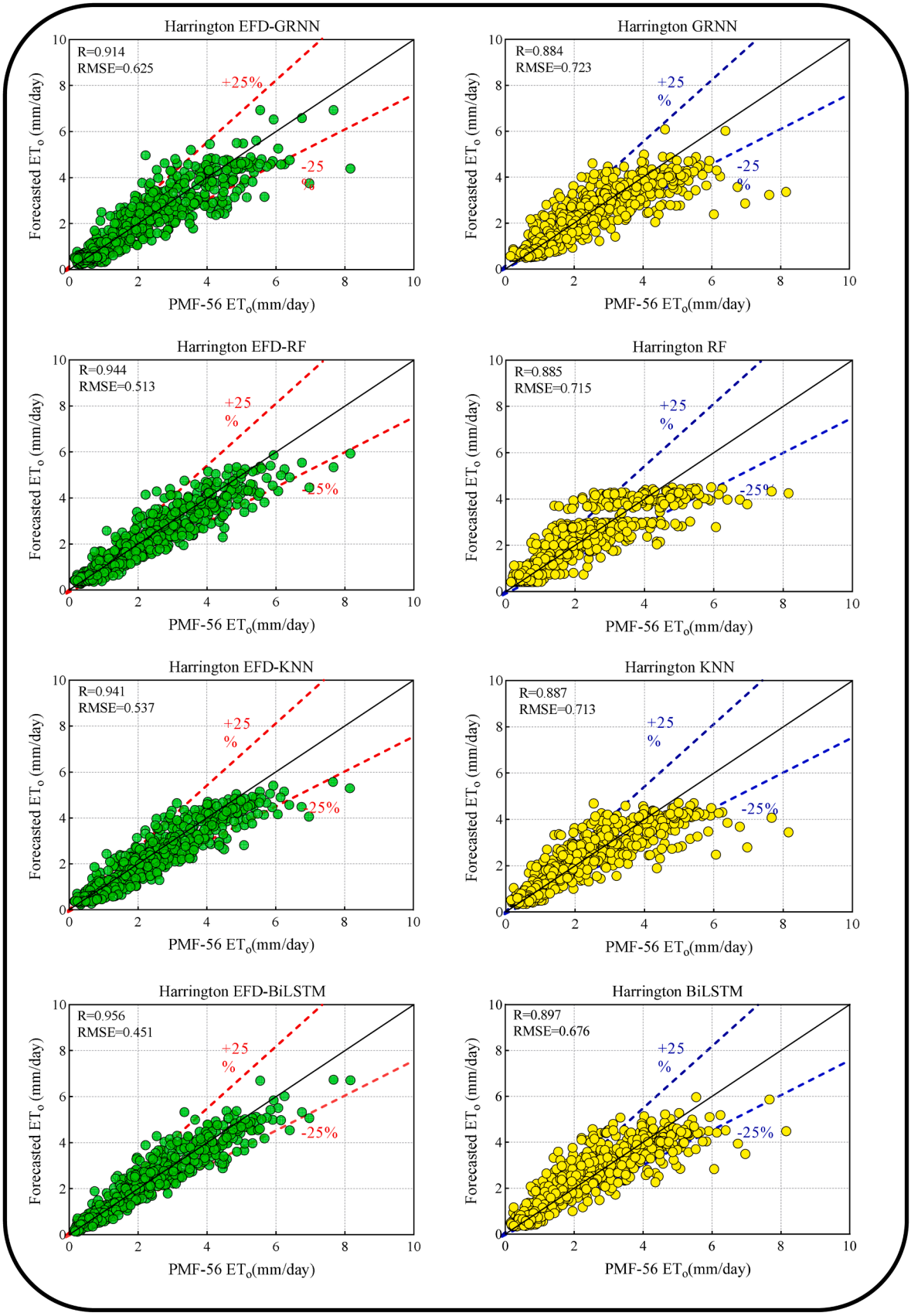

Fig. 10. Scatter plots of forecasted and measured ET$_o$ at Harrington station for one-step (day) forecasting.

Table 5
Evaluation metrics for one step ahead ET_o forecasting in St Peters station.

Model	Data	*R	RMSE (mm/day)	MAPE%	KGE	U_1	U_2	$U_{95\ \%}$
GRNN	Train	0.922	0.560	34.618	0.853	0.121	0.235	1.096
	Test	0.868	0.761	33.391	0.793	0.157	0.302	1.128
RF	Train	0.908	0.601	31.017	0.849	0.129	0.252	1.667
	Test	0.872	0.748	32.332	0.797	0.154	0.297	2.073
KNN	Train	0.886	0.668	33.799	0.816	0.144	0.280	1.851
	Test	0.869	0.761	32.660	0.775	0.158	0.303	2.108
BiLSTM	Train	0.884	0.672	34.820	0.840	0.143	0.282	1.862
	Test	0.881	0.724	32.643	0.827	0.147	0.288	2.006
EFD-GRNN	Train	0.982	0.271	19.799	0.957	0.057	0.114	0.531
	Test	0.909	0.651	27.064	0.856	0.134	0.259	0.794
EFD-RF	Train	0.990	0.208	10.248	0.952	0.044	0.087	0.578
	Test	0.917	0.619	25.899	0.863	0.127	0.246	1.704
EFD-KNN	Train	0.928	0.536	25.786	0.870	0.115	0.225	1.485
	Test	0.909	0.658	24.963	0.822	0.137	0.262	1.799
EFD-BiLSTM	Train	0.952	0.452	31.617	0.899	0.094	0.190	1.238
	Test	**0.956**	**0.451**	**22.218**	**0.914**	**0.091**	**0.179**	**1.249**

* R: Correlation Coefficient, RMSE: Root Mean Square Error, MAPE: Mean Absolute Percentage Error, U_1 and U_2: Theil's inequality coefficients, KGE: Kling Gupta Efficiency, U_{95} % uncertainty with 95% confidence.

$$MAPE = \frac{1}{N}\sum_{i=1}^{N}\left|\frac{ET_{o,i} - ET_{p,i}}{ET_{o,i}}\right| \times 100 \quad (17)$$

$$U1 = \frac{RMSE}{\sqrt{\frac{1}{N}\sum_{i=1}^{N} ET_{o,i}^2} + \sqrt{\frac{1}{N}\sum_{i=1}^{N} ET_{p,i}^2}} \quad (18)$$

$$KGE = 1 - \sqrt{(R-1)^2 + (\alpha-1)^2 + (\beta-1)^2} \quad (19)$$

$$U_2 = \frac{\sum_{i=1}^{N}\left(ET_{o,i} - ET_{p,i}\right)^2}{\sum_{i=1}^{N} ET_{o,i}^2} \quad (20)$$

$$U_{95\%} = 1.96\sqrt{Standard\ deviation^2 + RMSE^2} \quad (21)$$

Here, the values of the observed and forecasted reference evapotranspiration are $ET_{o,i}$ and $ET_{p,i}$, respectively. The entire amount of data is N. The Kling–Gupta efficiency (KGE) is an extensively employed goodness-of-fit indicator in the hydrologic sciences that facilitates the comparison between observations and simulations [45]. It should be emphasized that the α in KGE represents the fraction of the forecasted and observed average values, while the β stands for the comparative differences between the forecasted and actual values. R and KGE equal 1 for ideal model performance, whereas $MAPE$, $RMSE$, $U_{95\%}$, $U1$, and U_2 equal 0.

3. Results and discussion

Different metrics and various diagnostic plots were used to assess the accuracy of the hybrid and standalone models to forecast multi-step (days) ahead ETo in Harrington and St Peters stations. The standalone models are GRNN, RF, KNN, and BiLSTM, while their hybrid counterparts are EFD-GRNN, EFD-RF, EFD-KNN, and EFD-BiLSTM. All models were evaluated using several goodness-of-fit metrics to forecast multi-step (days) ahead of ET_o.

3.1. single step daily ET_o forecasting

Table 4 displays the goodness-of-fit metrics for one step ahead of ET_o forecasting in Harrington station to evaluate the performance of the standalone and hybrid versions of the models. The hybrid EFD-BiLSTM appeared to be the most accurate model in training and testing periods by reporting $R = 0.946$, RMSE = 0.466 mm/day for the training dataset and $R = 0.956$, RMSE = 0.451 mm/day for the test dataset. The EFD-BiLSTM model is ranked highest, followed by EFD-RF, EFD-GRNN, EFD-KNN, BiLSTM, RF, GRNN, and KNN models. Table 4 shows that the hybrid versions of the models are more precise in one-step ahead ET_o forecasting than their standalone counterpart models. This confirms that the EFD preprocessing technique enhances the forecasting accuracy of the models. However, overall, the EFD-BiLSTM shows better forecasting accuracy than all other models.

The comparison between the measured and forecasted one-step ahead ET_o, generated by all models, is inspected through scatter plots in Fig. 10 for the Harrington station during the testing period. Additionally, the R and RMS values can be observed in Fig. 10. The scatter plots deliver additional valuation of the forecasting capability of the models between the measured and forecasted ET_o. The EFD-BiLSTM model to forecast one-step ahead ET_o exhibited the highest precision with $R = 0.956$ and RMSE= 0.451 mm/day, followed by EFD-RF, EFD-GRNN, EFD-KNN, and standalone models. By comparing the hybrid and standalone, the scatter plots appeared to be more closed with the fit line within the 25 % upper and lower bound threshold. The scatter diagrams in Fig. 10 confirmed that EFD-BiLSTM is better in forecasting one step ahead of ET_o for Harrington station. As is apparent from Fig. 10, the application of the EFD technique and its combination with machine learning models has improved the performance, and its effect on the collection of points around the 1:1 line is clear. Also, a smaller number of points are outside the +/− 25% range lines. However, the comparison between different learning models shows that the BILSTM model has been able to predict the maximum evapotranspiration values with higher accuracy, and the two maximum points of evapotranspiration in test data are within the +/− 25% range lines. In the other three models, the endpoints are outside the 25 % error range, which indicates the better performance of the BiLSTM model.

The EFD-BiLSTM model also attained the highest accuracy values to forecast one step ahead of ET_o at the St Peters station, revealed in Table 5, as compared to other models. The EFD-BiLSTM model displayed the highest magnitude of $R = 0.952$, 0.956; RMSE = 0.452, 0.451 mm/day; MAPE = 31.617, 22.218 %; KGE = 0.899, 0.914; $U_1 = 0.094$, 0.091; $U_2 = 0.190$, 0.179; and $U_{95} = 1.238$, 1.249 in both training and testing periods respectively to forecast one-step ahead ET_o. This confirms again that the hybrid version of the models leads to better accuracy than the standalone models. But overall, the EFD-BiLSTM model demonstrated better performance than other hybrid and standalone models in forecasting ET_o for St Peters station one step ahead.

The scatter plots in Fig. 11 revealed the model's hybrid and standalone counterparts' comparison between the measured and forecasted ET_o along with R and RMSE values. The EFD-BiLSTM shows higher precision to forecast one-step ahead ET_o with higher $R = 0.956$ and RMSE = 0.451 mm/day as compared to EFD-RF, EFD-GRNN, EFD-KNN, BiLSTM, RF, GRNN, and KNN models for St Peters station. The EFD-

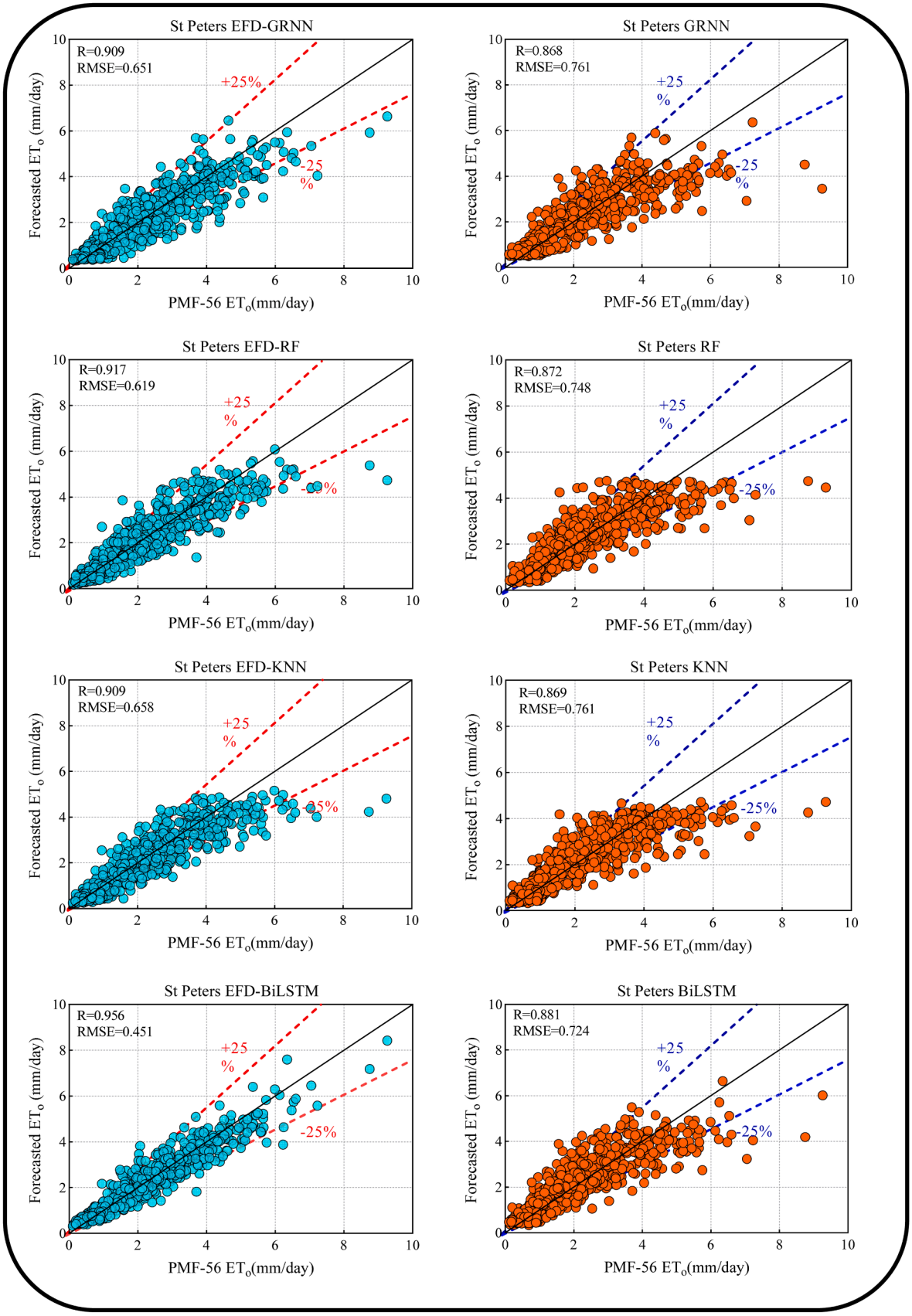

Fig. 11. Scatter plots of forecasted and measured ET_o at St Peter's station for one-step (day)forecasting.

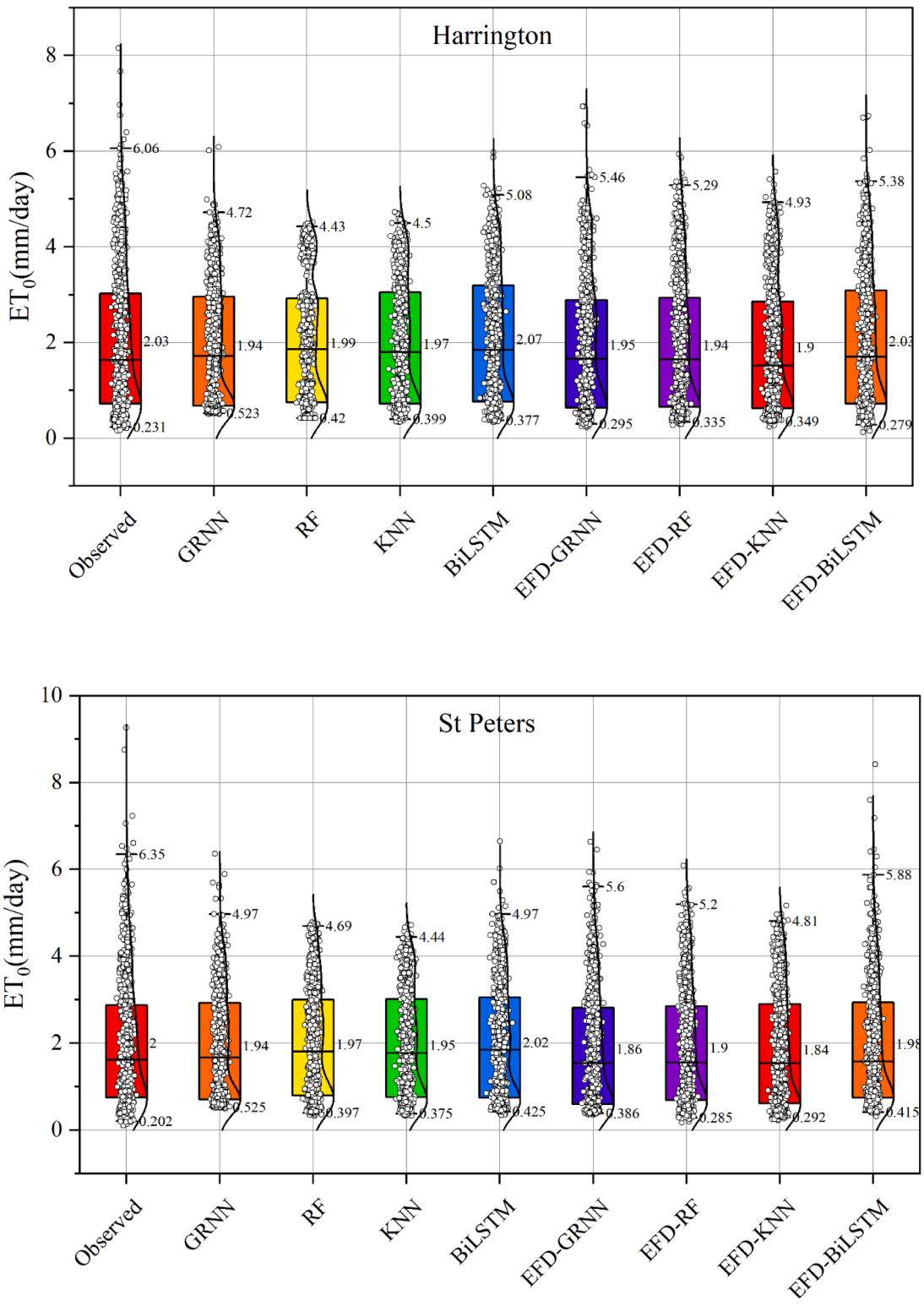

Fig. 12. Box plots and distribution of observed values of ET_o against model values for Harrington and St Peters stations.

BilSTM again presented better accuracy in terms of scatter plots to forecast one step ahead of ET_o as compared to other models. Here, too, a trend similar to Fig. 10 is observed, and the BILSTM model is able to predict the maximum points of evapotranspiration better than other models.

Fig. 12 describes the boxplots to provide a diagnostic analysis using the forecasted ET_o of EFD-BiLSTM, EFD-RF, EFD-GRNN, EFD-KNN, BiLSTM, RF, GRNN, and KNN models in relation to the observed ET_o for Harrington and St Peters stations. By observing Fig. 12, it is apparent that the EFD-BiLSTM model displayed more accurate boxplot distribution compared to the observed ET_o at both stations compared to all other benchmarking models. Also, the EFD-BILSTM model has been able to predict the higher evapotranspiration values with higher accuracy than other models. This proved that the EFD-BiLSTM model accomplishes accurate forecasts based on Fig. 12 for both Harrington and St Peters stations.

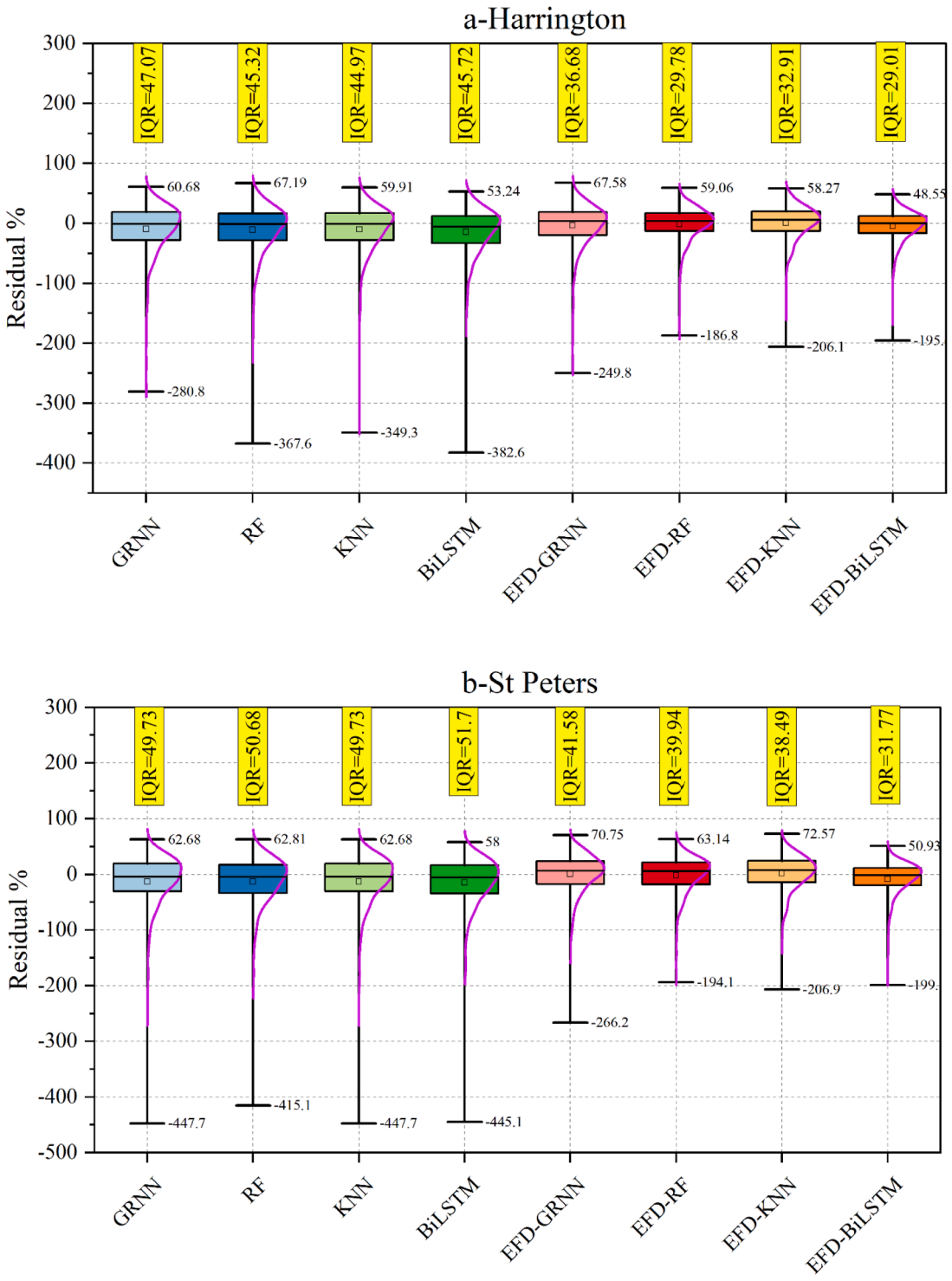

Fig. 13. Residual box plots for a) Harrington and b) St Peters stations.

The residual box plots for both Harrington and St Peters stations in Fig. 13 deliver a more tangible comparison of the models' forecasting capacity along with IQR values and the interquartile range using the hybrid EFD-BiLSTM vs. EFD-RF, EFD-GRNN, EFD-KNN, BiLSTM, RF, GRNN, and KNN models to forecast ET_o.The EFD-BiLSTM model presented a more accurate forecast with lower residual box plot distribution and a lower IQR = 29.01 (Harrington station) and 31.77 (St Peters station) to forecast ET_o as compared to all other models. Thus, EFD-BiLSTM models achieve accurate ET_o forecasting based on residual box plots for both stations.

The Taylor diagram in Fig. 14 discussed the observed and forecasted ET_o using EFD-BiLSTM, EFD-RF, EFD-GRNN, EFD-KNN, BiLSTM, RF, GRNN, and KNN to evaluate their precision for both Harrington and St Peters stations. These diagrams are considered an all-inclusive assessment to inspect the models' comparability based on standard deviation and correlation coefficient. For Harrington station, the EFD-BiLSTM model is located very closely to the observed ET_o by reporting a correlation coefficient between 0.95 and 0.99 with a standard deviation (1.25 to 1.50). The hybrid EFD-RF, EFD-GRNN, and EFD-KNN models are reasonably acceptable, but their forecasting accuracy could not surpass

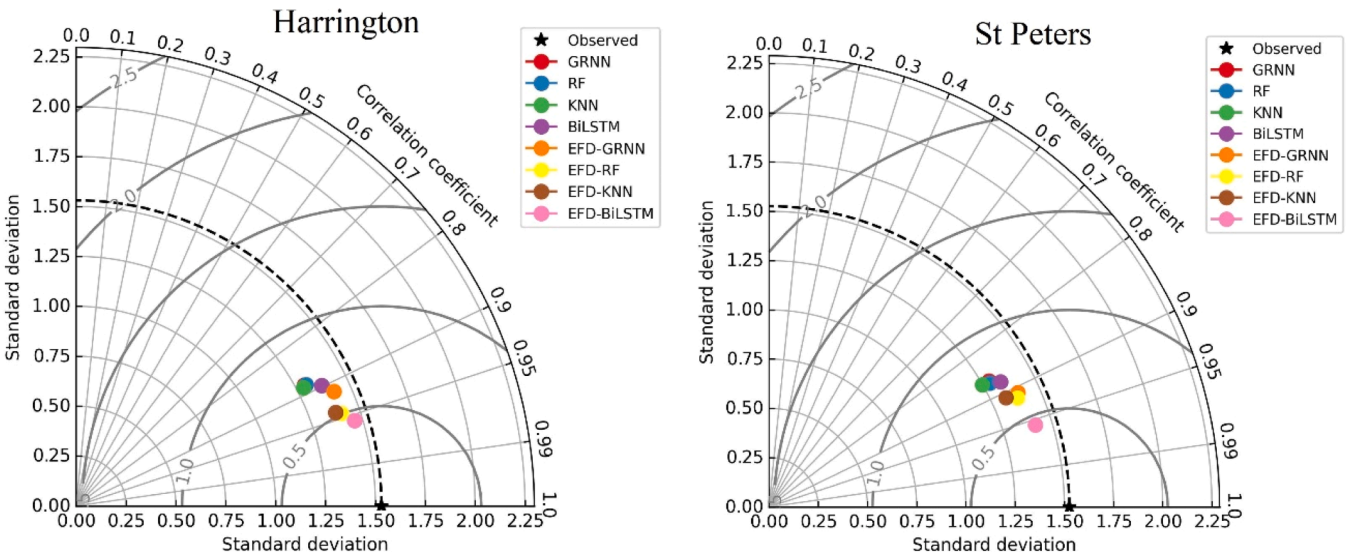

Fig. 14. Taylor diagrams for Harrington and St Peters stations.

Table 6
Evaluation Metrics for multi-step (days) ahead ET_o forecasting in Harrington station.

Model	Steps Ahead	Data	*R	RMSE (mm/day)	MAPE%	KGE	U1	U2	U95
Single	3	Train	0.855	0.739	36.357	0.805	0.163	0.317	2.050
		Test	0.853	0.800	33.716	0.789	0.163	0.315	2.217
	7	Train	0.824	0.808	39.703	0.778	0.178	0.346	2.240
		Test	0.844	0.823	33.850	0.782	0.168	0.324	2.282
	14	Train	0.804	0.854	52.276	0.747	0.184	0.365	2.359
		Test	0.833	0.850	44.483	0.750	0.171	0.334	2.353
	21	Train	0.800	0.854	54.453	0.720	0.188	0.365	2.368
		Test	0.803	0.913	49.156	0.699	0.187	0.359	2.533
EFD-based	3	Train	0.936	0.510	25.048	0.871	0.113	0.219	1.407
		Test	0.930	0.565	23.612	0.892	0.114	0.222	1.563
	7	Train	0.918	0.564	29.429	0.876	0.123	0.242	1.564
		Test	0.892	0.699	28.456	0.842	0.142	0.275	1.931
	14	Train	0.879	0.681	42.886	0.803	0.148	0.291	1.886
		Test	0.881	0.725	33.686	0.815	0.146	0.285	2.011
	21	Train	0.906	0.602	32.862	0.858	0.131	0.257	1.669
		Test	0.896	0.714	48.004	0.757	0.142	0.281	1.958

* R: Correlation Coefficient, RMSE: Root Mean Square Error, MAPE: Mean Absolute Percentage Error, U_1 and U_2: Theil's inequality coefficients, KGE: Kling Gupta Efficiency, U_{95} % uncertainty with 95% confidence.

the EFD-BiLSTM model. All the standalone BiLSTM, RF, GRNN, and KNN models lie far from the observed ET_o. The EFD-BiLSTM model again obtained a higher position in terms of accuracy for St Peters station in relation to other comparing models to forecast ET_o. The Taylor diagram thus depicts the appropriateness for better ET_o forecasting of the EFD-BiLSTM model.

3.2. *Multi-step (days) ahead forecasting for Harrington station*

Table 6 illustrates the multi-step (days) ahead ET_o forecasting in Harrington station to assess the performance accuracy of the hybrid EFD-BiLSTM against the standalone BiLSTM model. The EFD-BiLSTM appeared to be the most precise model for three days ahead of the ET_o forecast in terms of R, RMSE, MAPE, KGE, U_1, U_2, and U_{95} % metrics against the standalone BiLSTM model. Similarly, the EFD-BiLSTM shows better accuracy in terms of 7, 14, and 21 days ahead to forecast ET_o for Harrington station as compared to the standalone BiLSTM model. It is to be noted that the hybrid EFD-BiLSTM model accuracy is slightly lower in 14 days ahead as compared to the 3, 7, and 21 days ahead ET_o forecasting for Harrington station. Overall, the EFD-BiLSTM performs better than standalone BiLSTM for 3, 7, 14, and 21 days ahead ET) forecasting.

The bar graphs depicted in Fig. 15 demonstrate the R and RMSE values attained by the EFD-BiLSTM and standalone approaches at Harrington station for forecasting ET_o at 3, 7, 14, and 21 days ahead. The EFD-BiLSTM model exhibited the highest R values and the lowest RSME magnitudes in predicting ET_o for 3, 7, 14, and 21 days ahead, surpassing the standalone BiLSTM model. According to the bar graphs in Fig. 15, it was determined that the EFD-BiLSTM model demonstrates superior accuracy in predicting multi-step (days) ahead ET_o in comparison to the standalone BiLSTM model.

Fig. 16 represents the observed and forecasted values of 3, 7, 14, and 21 days ahead of ET_o using EFD-BiLSTM against the standalone BiLSTM model for Harrington station regarding scatter plots. Moreover, the R, in combination with the RMSE metric, was also incorporated in Fig. 8. The EFD-BiLSTM model at 3, 7, 14, and 21 days ahead of forecast ET_o displayed the highest precision with R and RMSE values in relation to the standalone BiLSTM model. The scatter diagram in Fig. 16 established that EFD-BiLSTM is better in forecasting multi-steps (days) ahead of ET_o Harrington station. However, it can be seen from Fig. 16 that increasing the forecasting horizon from 3 to 28 days leads to lower accuracy, especially in high evapotranspiration values. In 3 days ahead forecasting, the EFD-BiLSTM model succeeded in forecasting higher values, while in 7,14, and 21 days ahead, it underestimated the high evapotranspiration values.

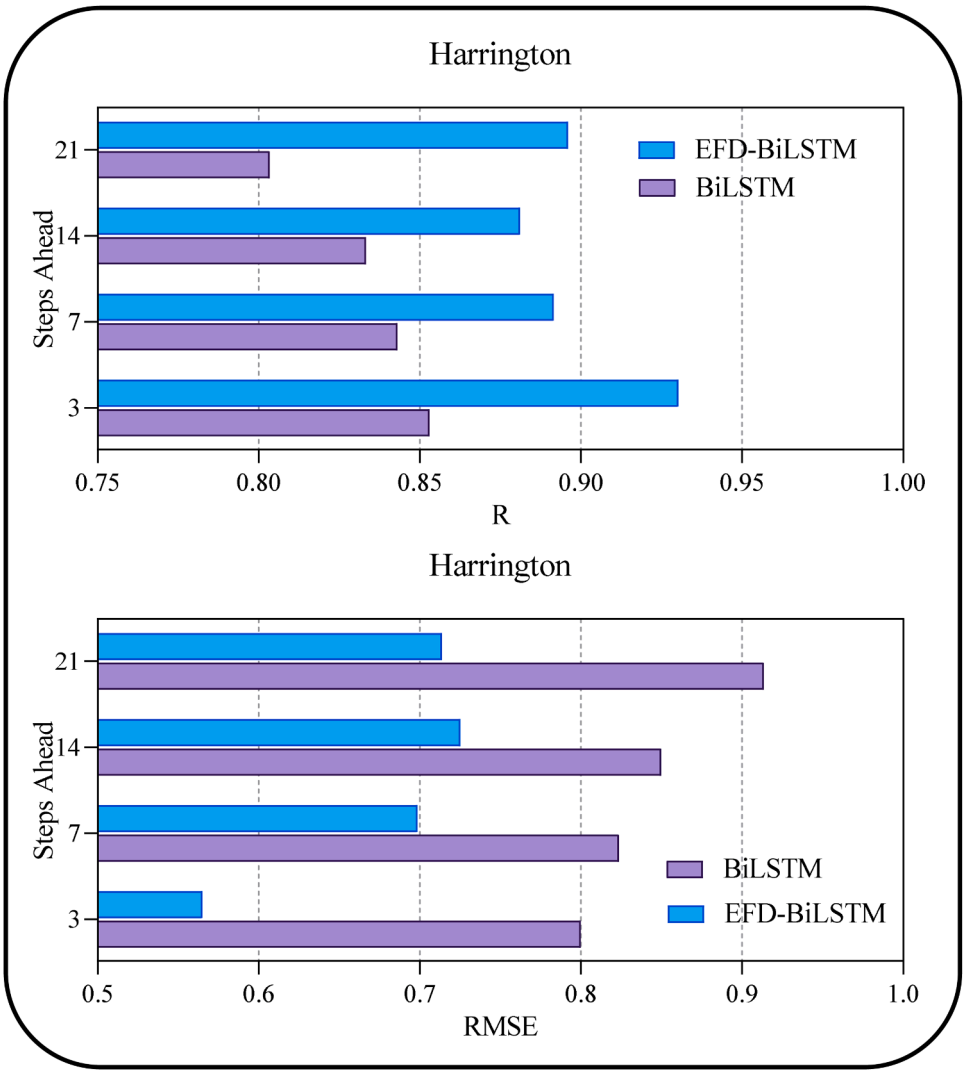

Fig. 15. Bar plots of multi-step (days) ahead forecasting of R and RMSE metrics for Harrington station.

3.3. Multi-step (days) ahead forecasting for St Peters station

The multi-step ahead (days) ET_o forecasting results are illustrated in Table 7 for St Peters station to assess the accuracy of the hybrid EFD-BiLSTM against the standalone BiLSTM model. The hybrid EFD-BiLSTM shows the highest precision based on the assessment metrics in training and testing periods for 3, 7, 14, and 21 days ahead of ET_o forecasting against the standalone counterpart BiLSTM model. The hybrid EFD-BiLSTM model shows better predictability for 3 and 7 days as compared to 14 and 21 days in St Peter station to forecast ET_o. It is also to be noted that multi-step (days) ahead ET_o forecasting is improved by EFD when combined with BiLSTM, confirming that EFD is a suitable preprocessing method. The EFD-BiLSTM model consistently achieved higher accuracy compared to the standalone BiLSTM for St Peter station when forecasting the ET_o for 3, 7, 14, and 21 days ahead.

The bar graphs portray the R and RMSE values achieved by the EFD-BilSTM and BiLSTM during the 3, 7, 14, and 21 days ahead forecasting ET_o in Fig. 17 for St Peters station. It is clear that the EFD-BiLSTM model generated the highest R scores and Lowest RMSE values to forecast 3, 7, 14, and 21 days ahead of ET_o compared with another benchmarking model, i.e., BiLSTM (see Fig. 17). The bar graphs thus prove that the EFD-BiLSTM exhibits higher accuracy in forecasting multi-steps (days) ahead of ET_o in St. Peters station.

Fig. 18 directly compares the observed and forecasted values of multi-step (days) ahead ET_o using EFD-BiLSTM and standalone BiLSTM model for St Peters station in terms of scatter plots along with R and RMSE metrics. The scatter plots presented here offer an additional evaluation of the predictive accuracy for the observed and forecasted ET_o at St. Peters station, at 3, 7, 14, and 21 days ahead. The EFD-BiLSTM model at 3, 7, 14, and 21 days ahead to forecast ET_o displayed the highest precision with R and RMSE compared to the BiLSTM model. Fig. 18 confirmed that EFD-BiLSTM is better in forecasting multi-step ahead ET_o for St Peter station. From Fig. 18, it can be concluded that all models underestimate the higher evapotranspiration values; however, EFD-based model errors are less than single models.

4. Further discussion

Wavelet transformations, a conventional technique for time series decomposition, have been extensively used with artificial intelligence models to estimate evapotranspiration (ETo). Gocić et al. [46] employed wavelet preprocessing in conjunction with artificial neural networks (ANN) and support vector regression (SVR), whereas Karbasi [47] integrated wavelets with Gaussian Process regression (GPR), both demonstrating improved performance compared to individual models. Araghi et al. [48] effectively utilized wavelet decomposition as an input for artificial neural networks (ANN) to forecast daily ETo.

Although wavelets offer some benefits in managing non-

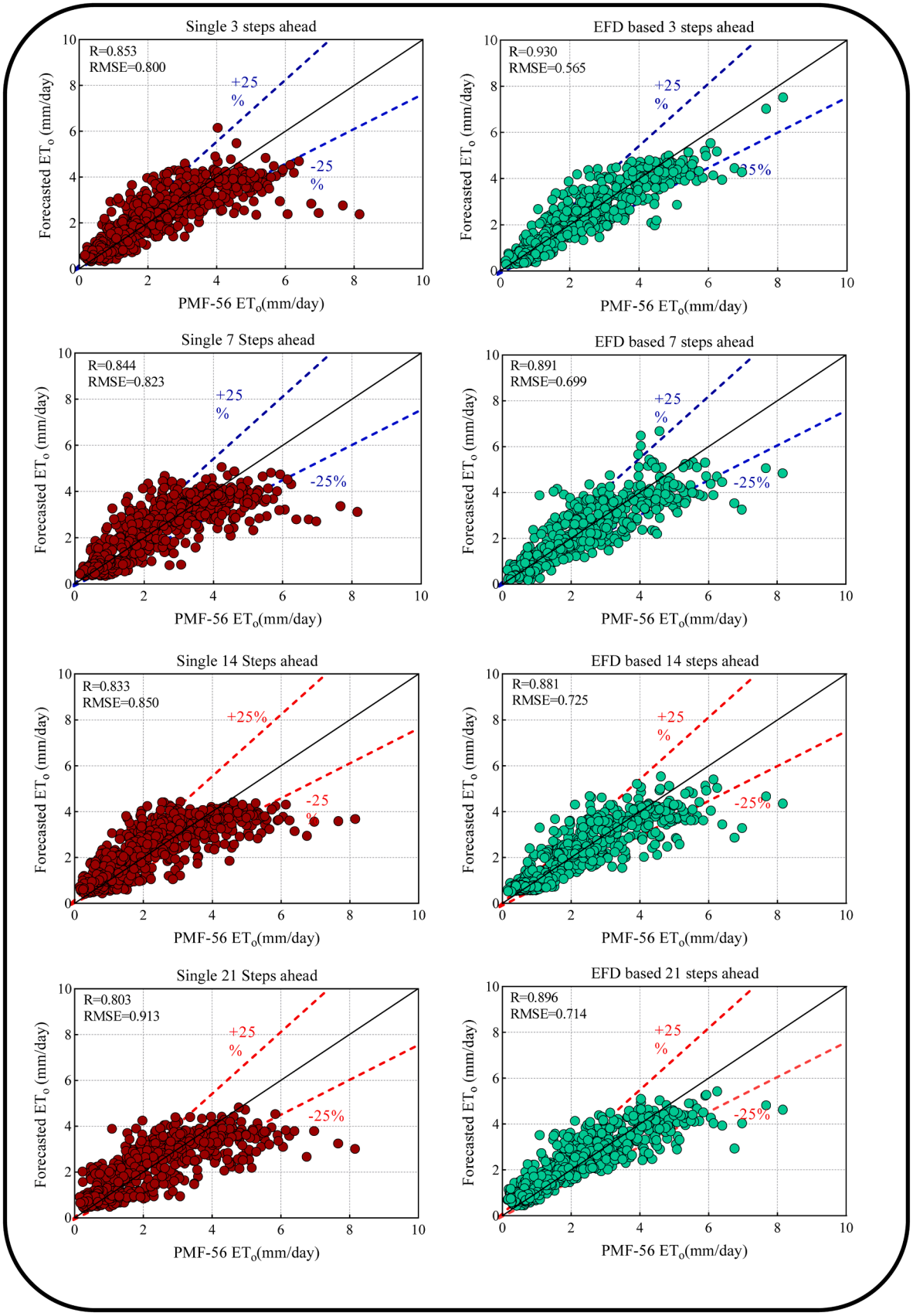

Fig. 16. Scatter plots of Forecasted and measured ET_o at Harrington station for multi-step (days) forecasting.

Table 7
Evaluation metrics for multi-step (days) ahead ET_o forecasting in St Peters station.

Model	Steps Ahead	Data	*R	RMSE (mm/day)	MAPE%	KGE	U1	U2	U95
Single	3	Train	0.833	0.795	41.099	0.783	0.170	0.334	2.203
		Test	0.828	0.856	38.242	0.760	0.175	0.341	2.374
	7	Train	0.803	0.857	45.412	0.750	0.183	0.359	2.375
		Test	0.816	0.882	39.605	0.737	0.181	0.351	2.445
	14	Train	0.791	0.878	48.803	0.713	0.190	0.367	2.435
		Test	0.792	0.933	42.561	0.701	0.193	0.371	2.587
	21	Train	0.769	0.918	56.142	0.689	0.197	0.383	2.543
		Test	0.784	0.948	50.393	0.681	0.196	0.377	2.627
EFD-based	3	Train	0.898	0.640	34.497	0.864	0.134	0.268	1.763
		Test	0.899	0.671	27.808	0.875	0.136	0.267	1.859
	7	Train	0.888	0.668	37.690	0.849	0.139	0.280	1.840
		Test	0.881	0.724	31.226	0.849	0.147	0.288	2.006
	14	Train	0.870	0.714	41.127	0.825	0.149	0.299	1.970
		Test	0.870	0.752	33.920	0.832	0.153	0.299	2.086
	21	Train	0.862	0.731	41.749	0.782	0.155	0.305	2.023
		Test	0.851	0.804	37.116	0.770	0.166	0.320	2.228

* R: Correlation Coefficient, RMSE: Root Mean Square Error, MAPE: Mean Absolute Percentage Error, U_1 and U_2: Theil's inequality coefficients, KGE: Kling Gupta Efficiency, U_{95} % uncertainty with 95% confidence.

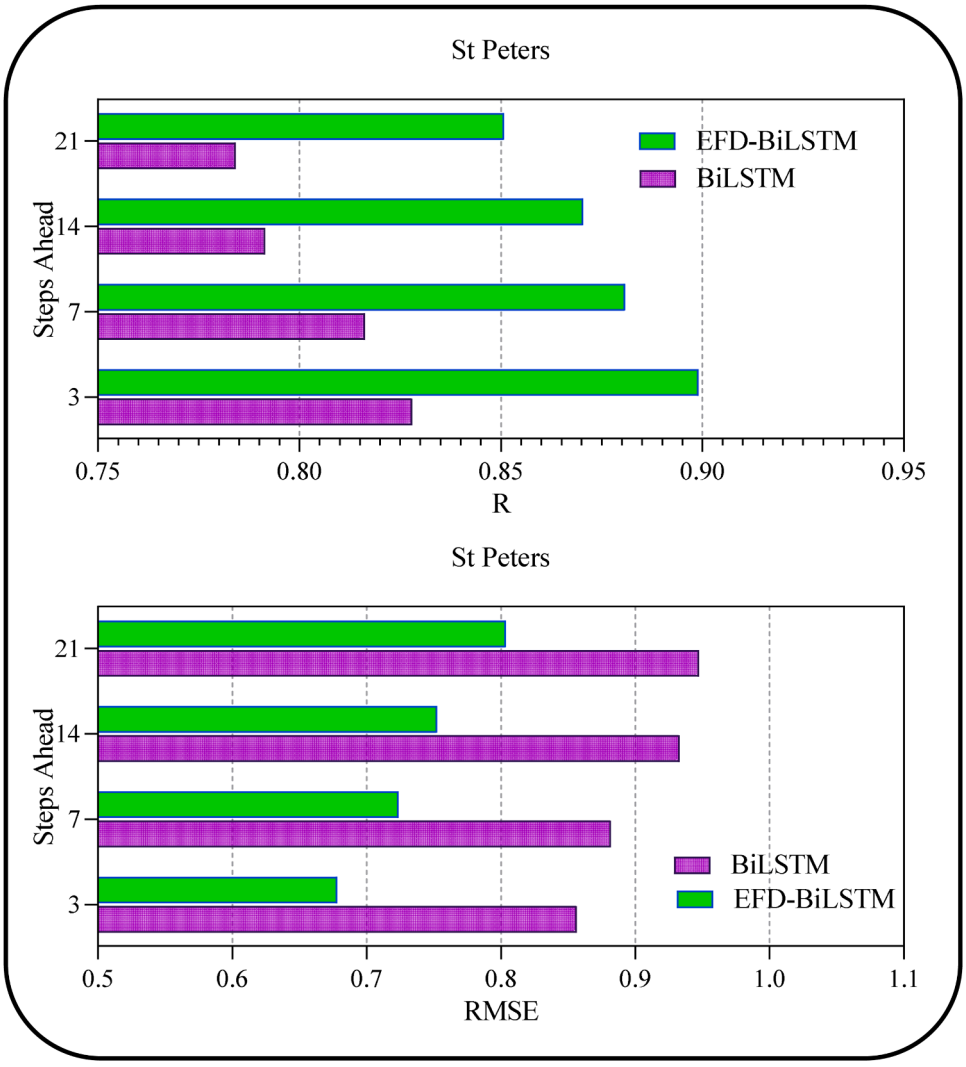

Fig. 17. Bar plots of multi-step (days) ahead forecasting of R and RMSE metrics for St Peters station.

stationarities, more sophisticated decomposition algorithms have been developed to enhance time-frequency localization accuracy. The empirical mode decomposition (EMD) and its variants, such as ensemble EMD (EEMD), have become increasingly popular. For example, Lu et al. [49] introduced a hybrid model that outperformed traditional methods for ETo prediction in China: the EEMD-BPNN (Back Propagation Neural Network).

In this research, the use of Empirical Fourier Decomposition (EFD)

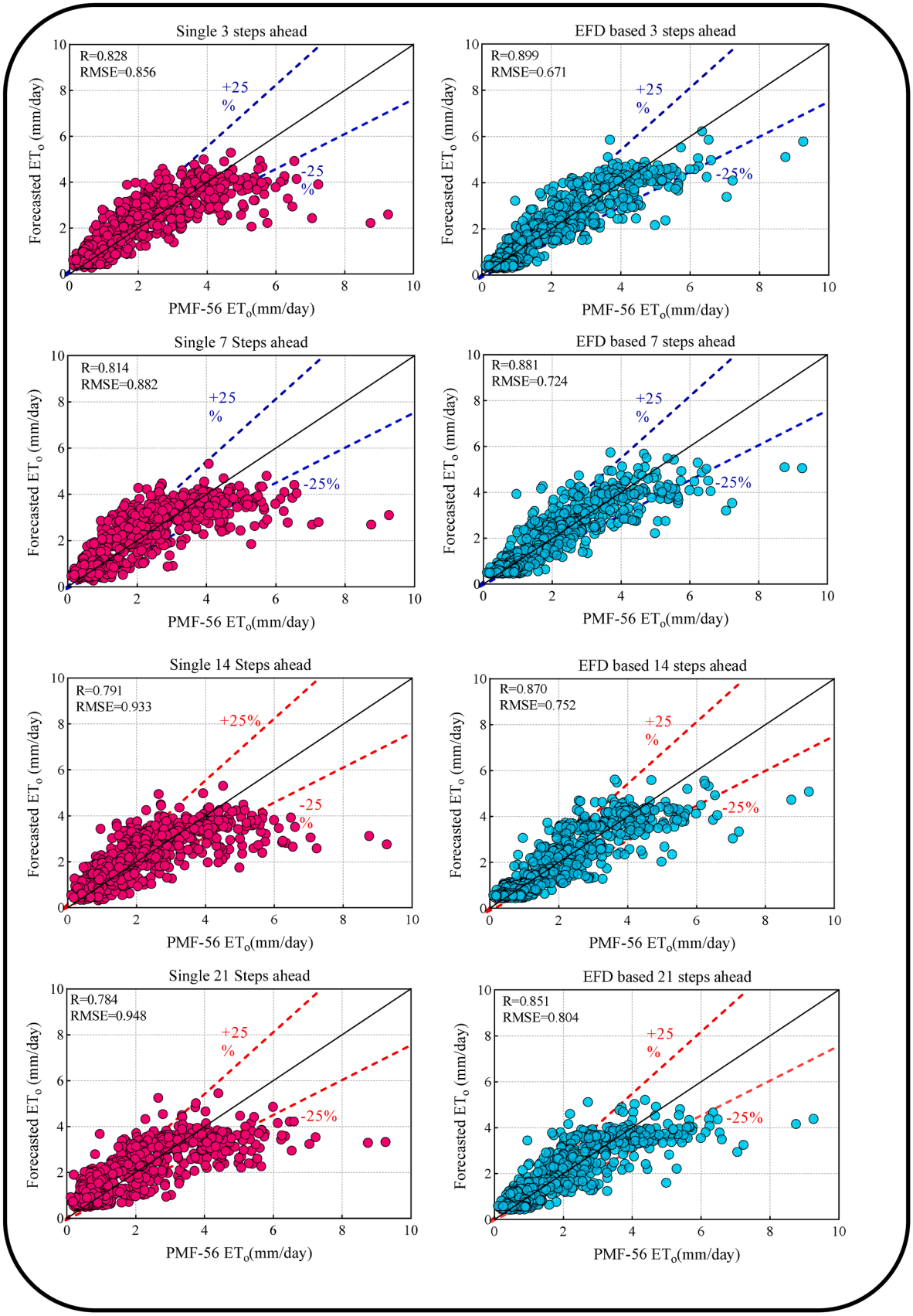

Fig. 18. Scatter plots of Forecasted and measured ET$_o$ at St Peters Station for multi-step (days) forecasting.

represents a significant improvement, addressing specific limitations of EMD/VMD related to mode mixing and inconsistent decompositions. The integration of Fourier spectral segmentation and filter banks in EFD results in a higher time-frequency resolution compared to wavelets and EMD versions. The EFD-BiLSTM-Kbest framework, which combines the powerful Bidirectional LSTM architecture with Kbest feature selection, demonstrated acceptable accuracy in forecasting long-term multi-temporal ET_o up to 28 days in advance. The degree of precision has been achieved one step ahead forecasting, with a Root Mean Square Error (RMSE) as low as 0.451 mm/day and correlation coefficients (R values) of 0.956. However, increasing the horizon of forecasting caused a decrease in accuracy, which many researchers have reported. The EFD method effectively captures localized time-frequency information in the non-stationary ETo signal, providing a strong basis for the deep learning model to learn complex patterns.

To advance the research, one viable area is the evaluation of the efficiency of several signal decomposition techniques with EFD in dealing with non-stationarity and non-linearity. For instance, multivariate variational mode decomposition [50] and multivariate empirical mode decomposition [51] should be used. Despite the fact that deep learning models have been proven to be quite effective, they offer nontransparent results, which makes the generated forecasts non-interpretable. Consequently, the use of explainable AI methods, including Local Interpretable Model-Agnostic Explanations (LIME) [52] and Shapley Additive explanations (SHAP) [53], should be considered to improve the interpretability of the results. In order to address some issues concerning the best setting of hyperparameters, it is recommended that different improved optimization techniques such as PSO, Q-PSO, genetic algorithm as well as firefly algorithm be employed to fine-tune hyperparameters in order to achieve high prediction accuracy. In addition, basing the hybrid models on a richer set of uncertainty evaluations and reliability analysis, like the BMA [54] is recommended. Finally, addressing the issue of data quality, it would be useful to integrate satellite-derived products since integrating satellite-based predictors has been found to greatly improve the authenticity of the EFD-BiLSTM model.

Although the suggested EFD-BiLSTM-Kbest architecture exhibits considerable potential, it is important to acknowledge several limitations. Initially, the investigation was confined to two meteorological stations located in Prince Edward Island, Canada. Validating its robustness will be further enhanced by expanding the geographical scope and examining model performance across varied climatic zones. This would entail using the model with data sets from areas of different climate regimes including the arid, tropical and continental climates. Another possible constraint is the utilization of the PMF-56 equation for determining reference ETo values, which might involve underlying assumptions or uncertainties. Enhancing the analysis might be achieved by cross-validating it using direct ETo data obtained from lysimeters or improved remote sensing products.

This proposed model in the current study may be incorporated in smart irrigation systems to enhance the water usage efficiency. Since ET_o is predicted accurately, farmers will be able to schedule irrigation, applying water only when and where it is most required. This results in water efficiency, low energy use in pumping, and minimal over watering which is unhealthy for crops and causes nutrient runoff and soil erosion. By using ET_o data, farmers can plan on what crop to plant, and when to plant the crops. In the areas with scarce water, the model helps farmers to select better crop varieties based on the water availability and thus farm yields and profit may be improved.

5. Conclusion

A novel data decomposition-based Empirical Fourier Decomposition (EFD) and Bidirectional LSTM (BiLSTM) model enhanced with Kbest feature selection were fused to design EFD-BiLSTM for multi-temporal evapotranspiration forecasting in PEI, Canada. The key novelty factors include the EFD, Kbest feature selection, and BiLSTM models into one topology to forecast the multi-step (days) ahead ET_o. Firstly, the EFD method decomposes the input predictor data into signals. Next, the most influential signals were chosen using the Kbest feature selection. Lastly, the selected signals were fed into the BiLSTM model to construct the EFD-BiLSTM framework to forecast multi-steps ahead of ET_o. The results recommend that the EFD-BiLSTM model displays higher accuracy in forecasting multi-step (days) ET_o ahead of the comparing models. The findings also suggested that the hybrid models outperformed the standalone models in terms of achieving higher accuracy.

Likewise, the EFD-BiLSTM model also produced higher accuracy for 3, 7, 14, and 21 days ahead of ET_o forecasting at both stations., to tackle the challenges of climate change. The ET_o forecast, which measures the quantity of water that has evaporated and transpired, is an essential parameter in agriculture for determining the water needs of crops. This aids farmers and producers in quantifying their crops' water needs, facilitating more efficient irrigation scheduling and ensuring optimal water utilization to prevent overwatering or underwatering. In addition, ET_o forecasting aids in water resource management, and the EFD-BiLSTM model can be tested in other areas of interest in environmental forecasting.

Ethics statement

Not applicable: This manuscript does not include human or animal research.

Funding acknowledgements

This work has been supported by the Natural Sciences and Engineering Research Council of Canada (NSERC) Discovery Grants [RGPIN-2022–03547 to G.S.R. and to RGPIN-2023–03,351 to A.A.F.]. The authors thank the Atlantic Canada Opportunities Agency and NSERC Alliance for supporting this research. The authors are also gratful to the Precision Agriculture Research Group at the University of Prince Edward Island for their assistance.

CRediT authorship contribution statement

Masoud Karbasi: Writing – review & editing, Writing – original draft, Visualization, Software, Methodology, Formal analysis, Data curation, Conceptualization. **Mumtaz Ali:** Writing – review & editing, Writing – original draft, Validation, Supervision, Investigation. **Gurjit S. Randhawa:** Writing – review & editing, Validation, Supervision, Investigation, Funding acquisition. **Mehdi Jamei:** Writing – review & editing, Writing – original draft, Validation, Methodology. **Anurag Malik:** Writing – review & editing, Writing – original draft, Methodology. **Syed Hamid Hussain Shah:** Writing – review & editing, Visualization, Validation. **Melanie Bos:** Writing – review & editing, Visualization, Validation. **Qamar Zaman:** Writing – review & editing, Writing – original draft, Validation, Supervision, Project administration. **Aitazaz Ahsan Farooque:** Writing – review & editing, Validation, Supervision, Resources, Project administration, Investigation, Funding acquisition.

Declaration of competing interest

The authors declare the following financial interests/personal relationships which may be considered as potential competing interests:

Gurjit S. Randhawa reports financial support was provided by Natural Sciences and Engineering Research Council of Canada. Aitazaz Ahsan Farooque reports financial support was provided by Natural Sciences and Engineering Research Council of Canada. If there are other authors, they declare that they have no known competing financial interests or personal relationships that could have appeared to influence the work reported in this paper.

Acknowledgment

The authors express their gratitude to Environment Canada for their provision of meteorological data pertaining to the research sites, which were utilized to estimate the reference evapotranspiration and other predictor data.

Data availability

The data used in the manuscript is public. The manuscript has information on availability and access to the data.

References

[1] R.G. Allen, L.S. Pereira, D. Raes, M. Smith, Crop evapotranspiration-Guidelines for computing crop water requirements-FAO Irrigation and drainage paper 56, Fao, Rome 300 (9) (1998) D05109.
[2] R.G. Allen, L.S. Perieira, D. Raes, and M. Smith, "Irrigation and Drainage Paper Crop No. 56," no. 56, 2006.
[3] A.Pandey Darshana, R.P. Pandey, Analysing trends in reference evapotranspiration and weather variables in the Tons River Basin in Central India, Stoch. Environ. Res. risk Assess. 27 (2013) 1407–1421.
[4] L.S. Pereira, R.G. Allen, M. Smith, D. Raes, Crop evapotranspiration estimation with FAO56: past and future, Agric. Water Manag. 147 (2015) 4–20.
[5] C.P. Webb, Bureau of Meteorology Reference Evapotranspiration Calculations, Climate Services Centre, Queensland Regional Office, Bureau of Meteorology, 2010.
[6] M. Karbasi, et al., Development of an enhanced bidirectional recurrent neural network combined with time-varying filter-based empirical mode decomposition to forecast weekly reference evapotranspiration, Agric. Water Manag. 290 (Dec. 2023) 108604, https://doi.org/10.1016/j.agwat.2023.108604.
[7] A. Ahmadi, A. Daccache, M. Sadegh, R.L. Snyder, Statistical and deep learning models for reference evapotranspiration time series forecasting: a comparison of accuracy, complexity, and data efficiency, Comput. Electron. Agric. 215 (2023) 108424.
[8] A.R. Troncoso-García, I.S. Brito, A. Troncoso, F. Martínez-Álvarez, Explainable hybrid deep learning and Coronavirus Optimization Algorithm for improving evapotranspiration forecasting, Comput. Electron. Agric. 215 (2023) 108387.
[9] X. Zhao, et al., Exploring interpretable and non-interpretable machine learning models for estimating winter wheat evapotranspiration using particle swarm optimization with limited climatic data, Comput. Electron. Agric. 212 (2023) 108140.
[10] P. Goyal, S. Kumar, R. Sharda, A review of the Artificial Intelligence (AI) based techniques for estimating reference evapotranspiration: current trends and future perspectives, Comput. Electron. Agric. (2023), https://doi.org/10.1016/j.compag.2023.107836.
[11] G. Landeras, A. Ortiz-Barredo, J.J. López, Forecasting weekly evapotranspiration with ARIMA and artificial neural network models, J. Irrig. Drain. Eng. 135 (3) (2009) 323–334.
[12] S.W. Muthee, et al., Using the SARIMA model to predict the trends of evapotranspiration and runoff in the Muringato river basin, Kenya, Stoch. Environ. Res. Risk Assess. 37 (12) (2023) 4707–4718.
[13] S.D. Gorantiwar, D.T. Meshram, H.K. Mittal, Seasonal ARIMA model for generation and forecasting evapotranspirtion of Solapur district of Maharashtra, J. Agrometeorol. 13 (2) (2011) 119–122.
[14] O. Kisi, Evapotranspiration modelling from climatic data using a neural computing technique, Hydrol. Process. An Int. J. 21 (14) (2007) 1925–1934.
[15] T. Partal, Modelling evapotranspiration using discrete wavelet transform and neural networks, Hydrol. Process. An Int. J. 23 (25) (2009) 3545–3555.
[16] A. El-Shafie, H.M. Alsulami, H. Jahanbani, A. Najah, Multi-lead ahead prediction model of reference evapotranspiration utilizing ANN with ensemble procedure, Stoch. Environ. Res. Risk Assess. 27 (2013) 1423–1440.
[17] S. Siami-Namini, N. Tavakoli, A.S. Namin, The performance of LSTM and BiLSTM in forecasting time series, in: 2019 IEEE International conference on big data (Big Data), IEEE, 2019, pp. 3285–3292.
[18] K.U. Jaseena, B.C. Kovoor, Decomposition-based hybrid wind speed forecasting model using deep bidirectional LSTM networks, Energy Convers. Manag. 234 (November 2020) (2021) 113944, https://doi.org/10.1016/j.enconman.2021.113944.
[19] M. Schuster, K.K. Paliwal, Bidirectional recurrent neural networks, IEEE Trans. Signal Process. 45 (11) (1997) 2673–2681, https://doi.org/10.1109/78.650093.
[20] A. Emadi, R. Sobhani, H. Ahmadi, A. Boroomandnia, S. Zamanzad-Ghavidel, H. M. Azamathulla, Multivariate modeling of agricultural river water abstraction via novel integrated-wavelet methods in various climatic conditions, Environ. Dev. Sustain. (2022) 1–27.
[21] Ö. Kişi, Evapotranspiration modeling using a wavelet regression model, Irrig. Sci. 29 (2011) 241–252.
[22] W.-G. Wang, Y.-F. Luo, Wavelet network model for reference crop evapotranspiration forecasting, in: 2007 International Conference on Wavelet Analysis and Pattern Recognition, IEEE, 2007, pp. 751–755.
[23] W. Zhou, Z. Feng, Y.F. Xu, X. Wang, H. Lv, Empirical Fourier decomposition: an accurate signal decomposition method for nonlinear and non-stationary time series analysis, Mech. Syst. Signal Process. 163 (Jan. 2022) 108155, https://doi.org/10.1016/j.ymssp.2021.108155.
[24] B. Kumar, N. Yadav, A novel hybrid algorithm based on Empirical Fourier decomposition and deep learning for wind speed forecasting, Energy Convers. Manag. 300 (2024) 117891.
[25] M. Jamei, et al., Short-term drought Index forecasting for hot and semi-humid climate Regions: a novel empirical Fourier decomposition-based ensemble Deep-Random vector functional link strategy, Comput. Electron. Agric. 217 (2024) 108609.
[26] J. Maqsood, A.A. Farooque, X. Wang, F. Abbas, B. Acharya, H. Afzaal, Contribution of climate extremes to variation in potato tuber yield in Prince Edward Island, Sustainability 12 (12) (2020) 4937.
[27] A. and A.-F. Canada, "Potato Market Information Review," 2022. [Online]. Available: https://agriculture.canada.ca/en/sector/horticulture/reports/potato-market-information-review-2021-22.
[28] F. Pedregosa, et al., Scikit-learn: machine learning in Python, J. Mach. Learn. Res. 12 (2011) 2825–2830.
[29] T. Imbeault-Nepton, J. Maitre, K. Bouchard, S. Gaboury, Filtering Data Bins of UWB Radars for Activity Recognition with Random Forest, Procedia Comput. Sci. 201 (2022) 48–55.
[30] M.S. Zulfiker, N. Kabir, A.A. Biswas, T. Nazneen, M.S. Uddin, An in-depth analysis of machine learning approaches to predict depression, Curr. Res. Behav. Sci. 2 (2021) 100044.
[31] A. Graves, J. Schmidhuber, Framewise phoneme classification with bidirectional LSTM and other neural network architectures, Neural Networks 18 (5–6) (Jul. 2005) 602–610, https://doi.org/10.1016/j.neunet.2005.06.042.
[32] H. Kang, S. Yang, J. Huang, J. Oh, Time Series Prediction of Wastewater Flow Rate by Bidirectional LSTM Deep Learning, Int. J. Control. Autom. Syst. 18 (12) (Dec. 2020) 3023–3030, https://doi.org/10.1007/s12555-019-0984-6.
[33] I.K. Ihianle, A.O. Nwajana, S.H. Ebenuwa, R.I. Otuka, K. Owa, M.O. Orisatoki, A Deep Learning Approach for Human Activities Recognition From Multimodal Sensing Devices, IEEE Access 8 (2020) 179028–179038, https://doi.org/10.1109/ACCESS.2020.3027979.
[34] R. Rooki, Application of general regression neural network (GRNN) for indirect measuring pressure loss of Herschel–Bulkley drilling fluids in oil drilling, Measurement 85 (2016) 184–191.
[35] L. Breiman, Random forests, Mach. Learn. 45 (1) (2001) 5–32.
[36] L.B. Ferreira, F.F. da Cunha, New approach to estimate daily reference evapotranspiration based on hourly temperature and relative humidity using machine learning and deep learning, Agric. Water Manag. (2020), https://doi.org/10.1016/j.agwat.2020.106113.
[37] J. Fan, et al., Evaluation of SVM, ELM and four tree-based ensemble models for predicting daily reference evapotranspiration using limited meteorological data in different climates of China, Agric. For. Meteorol. 263 (July) (Dec. 2018) 225–241, https://doi.org/10.1016/j.agrformet.2018.08.019.
[38] H. Tyralis, G. Papacharalampous, A. Langousis, A brief review of random forests for water scientists and practitioners and their recent history in water resources, Water (Basel) 11 (5) (2019) 910.
[39] N.S. Altman, An introduction to kernel and nearest-neighbor nonparametric regression, Am. Stat. 46 (3) (1992) 175–185.
[40] A. Sumayli, Development of advanced machine learning models for optimization of methyl ester biofuel production from papaya oil: gaussian process regression (GPR), multilayer perceptron (MLP), and K-nearest neighbor (KNN) regression models, Arab. J. Chem. 16 (7) (2023) 104833.
[41] Z. Zheng, et al., Design data decomposition-based reference evapotranspiration forecasting model: a soft feature filter based deep learning driven approach, Eng. Appl. Artif. Intell. 121 (2023) 105984.
[42] F. Bliemel, Theil's Forecast Accuracy coefficient: A clarification, SAGE Publications Sage CA, Los Angeles, CA, 1973.
[43] H.V. Gupta, H. Kling, On typical range, sensitivity, and normalization of Mean Squared Error and Nash-Sutcliffe Efficiency type metrics, Water Resour. Res. 47 (10) (2011).
[44] H.V. Gupta, H. Kling, K.K. Yilmaz, G.F. Martinez, Decomposition of the mean squared error and NSE performance criteria: implications for improving hydrological modelling, J. Hydrol. 377 (1–2) (2009) 80–91.
[45] M.A. Ghorbani, M.A. Jabehdar, Z.M. Yaseen, S. Inyurt, Solving the pan evaporation process complexity using the development of multiple mode of neurocomputing models, Theor. Appl. Climatol. (2021), https://doi.org/10.1007/s00704-021-03724-8.
[46] M. Gocić, et al., Soft computing approaches for forecasting reference evapotranspiration, Comput. Electron. Agric. 113 (2015) 164–173.
[47] M. Karbasi, Forecasting of Multi-Step Ahead Reference Evapotranspiration Using Wavelet- Gaussian Process Regression Model, Water Resour. Manag. 32 (3) (2018), https://doi.org/10.1007/s11269-017-1853-9.
[48] A. Araghi, J. Adamowski, C.J. Martinez, Comparison of wavelet-based hybrid models for the estimation of daily reference evapotranspiration in different climates, J. Water Clim. Chang. 11 (1) (2020) 39–53.
[49] Y. Lu, T. Li, H. Hu, X. Zeng, Short-term prediction of reference crop evapotranspiration based on machine learning with different decomposition methods in arid areas of China, Agric. Water Manag. 279 (2023) 108175.
[50] N. ur Rehman, H. Aftab, Multivariate variational mode decomposition, IEEE Trans. Signal Process. 67 (23) (2019) 6039–6052.
[51] N. Rehman, D.P. Mandic, Multivariate empirical mode decomposition, Proc. R. Soc. A Math. Phys. Eng. Sci. 466 (2117) (2010) 1291–1302.

[52] S. Mishra, B.L. Sturm, S. Dixon, Local interpretable model-agnostic explanations for music content analysis, in: ISMIR, 2017, pp. 537–543.
[53] L.S. Shapley, A Value for n-Person Games, in: Contributions to the Theory of Games (AM-28), Volume II, Princeton University Press, 1953, pp. 307–318, https://doi.org/10.1515/9781400881970-018.
[54] J.M. Sloughter, T. Gneiting, A.E. Raftery, Probabilistic wind speed forecasting using ensembles and Bayesian model averaging, J. Am. Stat. Assoc. 105 (489) (2010) 25–35.